

A Subpixel Target Detection Approach to Hyperspectral Image Classification

Bai Xue, *Student Member, IEEE*, Chunyan Yu, *Member, IEEE*, Yulei Wang, Meiping Song, Sen Li, Lin Wang, Hsian-Min Chen, and Chein-I Chang, *Life Fellow, IEEE*

Abstract—Hyperspectral image classification faces various levels of difficulty due to the use of different types of hyperspectral image data. Recently, spectral–spatial approaches have been developed by jointly taking care of spectral and spatial information. This paper presents a completely different approach from a subpixel target detection view point. It implements four stage processes, a preprocessing stage, which uses band selection (BS) and nonlinear band expansion, referred to as BS-then-nonlinear expansion (BSNE), a detection stage, which implements constrained energy minimization (CEM) to produce subpixel target maps, and an iterative stage, which develops an iterative CEM (ICEM) by applying Gaussian filters to capture spatial information, and then feeding the Gaussian-filtered CEM-detection maps back to BSNE band images to reprocess CEM in an iterative manner. Finally, in the last stage Otsu’s method is applied to converting ICEM-detected real-valued maps to discrete values for classification. The entire process is called BSNE-ICEM. Experi-

mental results demonstrate BSNE-ICEM, which has advantages over support vector machine-based approaches in many aspects, such as easy implementation, fewer parameters to be used, and better false classification and precision rates.

Index Terms—Band expansion (BE), band ratio expansion process (BREP), band selection (BS), BS-then-nonlinear expansion (BSNE), constrained energy minimization (CEM), correlation BE process (CBEP), hyperspectral image classification, iterative CEM (ICEM), nonlinear BE process (NBEP), Otsu’s method, overall accuracy (OA), precision rate, support vector machine (SVM).

I. INTRODUCTION

HYPERSPECTRAL image classification has received considerable interest in recent years, e.g., see [1]–[13]. A general approach is spectral–spatial-based approaches, which use a pixel-based spectral classifier, such as support vector machine (SVM), to perform spectral classification coupled with spatial domain-based techniques to capture spatial contextual information, such as extended morphological profiles [2], to take care of both spectral and spatial correlation. While such a spectral–spatial approach seems promising, there are also some issues needed to be addressed. First of all, a pure-pixel-based spectral classifier does not take full advantage of mixing properties of a single pixel. Second, the used performance evaluation criterion, overall accuracy (OA) or average accuracy (AA), or kappa coefficient (κ) cannot sufficiently address classification issues, such as background (BKG) issue. Third, misclassification was not considered for performance analysis. Finally and most importantly, the classification performance is done by cross validation with the training and test samples being selected from the same class in different percentiles. As a result, no misclassified data samples from other classes are considered as falsely classified data samples. This leads to an issue that falsely misclassified rate is not included for classification evaluation.

This paper takes an approach from a subpixel target detection point of view, which is completely different from SVM-based approaches in [1], [5], [11], and [12]. In subpixel target detection, a detector makes soft decisions by finding real-valued abundance fractions of material substances present in a pixel, which can be used for target detection. As a result, such a subpixel target detection requires a threshold parameter τ to determine if a detected data sample is considered to be a target pixel. This property allows a detector to be used for binary classification. More specifically, if we consider a class of interest as a desired target to be detected which can be represented by the alternative hypothesis, H_1 , and all other classes as an undesired class, referred to as

Manuscript received October 18, 2016; revised January 27, 2017 and April 25, 2017; accepted April 28, 2017. Date of publication August 4, 2017; date of current version August 25, 2017. This work was supported by Fundamental Research Funds for Central Universities under Grant 3132016331, Grant 3132017124, and Grant 3132017080. The work of Y. Wang was supported by LSIT201707D. The work of M. Song was supported by the National Nature Science Foundation of China under Grant 61601077. The work of L. Wang was supported by the 111 Project under Grant B17035. (*Corresponding author: Chunyan Yu.*)

B. Xue is with the Center for Hyperspectral Imaging in Remote Sensing and the Information and Technology College, Dalian Maritime University, Dalian, China, and also with the Remote Sensing Signal and Image Processing Laboratory, Department of Computer Science and Electrical Engineering, University of Maryland, Baltimore County, Baltimore, MD 21250 USA (e-mail: baixue1@umbc.edu).

C. Yu and S. Li are with the Center for Hyperspectral Imaging in Remote Sensing and the Information and Technology College, Dalian Maritime University, Dalian, China (e-mail: 36202986@qq.com; listen@dlmu.edu.cn).

Y. Wang is with the Center for Hyperspectral Imaging in Remote Sensing the Information and Technology College, Dalian Maritime University, Dalian, China, and also with the Key Laboratory of Spectral Imaging Technology, Chinese Academy of Sciences, Xi’an, China (e-mail: wangyulei.wyl@163.com).

M. Song is with the Center for Hyperspectral Imaging in Remote Sensing, Information and Technology College, Dalian Maritime University, Dalian, China, and also with the State Key Laboratory of Integrated Services Networks, Xi’an, China (e-mail: smping@163.com).

L. Wang is with the School of Physics and Optoelectronic Engineering, Xidian University, Xi’an, China (e-mail: lwang@mail.xidian.edu.cn).

H.-M. Chen is with the Department of Medical Research, Taichung Veterans General Hospital, Taichung, Taiwan (e-mail: hsm6511@gmail.com).

C.-I Chang is with the Center for Hyperspectral Imaging in Remote Sensing, Information and Technology College, Dalian Maritime University, Dalian, China, also with the Remote Sensing Signal and Image Processing Laboratory, Department of Computer Science and Electrical Engineering, University of Maryland, Baltimore County, Baltimore, MD 21250 USA, and also with the Department of Computer Science and Information Management, Providence University, Taichung 02912, Taiwan (e-mail: cchang@umbc.edu).

Color versions of one or more of the figures in this paper are available online at <http://ieeexplore.ieee.org>.

Digital Object Identifier 10.1109/TGRS.2017.2702197

BKG class which can be represented by the null hypothesis, H_0 , then a detector designed for binary hypothesis testing problem becomes a binary classifier, which determines if a data sample belongs to either signal class or BKG class. The key difference is that a detector finds a boundary between two classes compared to a binary classifier, which assigns class membership to each of data samples. From an image processing point of view, a detector is actually an edge detector, while a binary classifier is essentially a thresholding technique, which partitions an image into foreground and BKG classes. With this interpretation, a detector can be performed as a binary classification to do what a two-class SVM does. It has been shown in [14]–[18] that the constrained energy minimization (CEM) is a promising and effective subpixel target detector for hyperspectral imagery. So, this suggests that CEM can also be considered as a binary classifier with only difference in that CEM is a soft detector while SVM is a hard classifier. Furthermore, to cope with nonlinear separability problems, SVM uses nonlinear kernels. Since CEM is also a linear filter, in order for CEM to do the same, we introduce a new concept of band selection-then-nonlinear expansion (BSNE), which first selects a set of appropriate bands, and then nonlinearly expands the selected band subset to form a new hyperspectral image. This BSNE plays a similar role as a kernel does for SVM. Additionally, due to the fact that SVM is a pixel-based spectral classifier, a spectral-spatial approach generally employs a follow-up spatial filter to obtain spatial contextual information. Following a similar idea CEM also applies Gaussian filters to CEM-detection maps to capture spatial information, and then feeds back the Gaussian-filtered images to BSNE band-expanded images repeatedly. The more feedbacks the Gaussian filter images to be added to BSNE band-expanded images, the more the spatial information included. The type of CEM using feedback loops to include spatial information via Gaussian-filtered images is called iterative CEM (ICEM). Also ICEM using BSNE to generate nonlinear band images is called BSNE-ICEM. Accordingly, BSNE-ICEM can accomplish what a spectral-spatial approach can for hyperspectral image classification.

In general, to evaluate a spectral-spatial approach, $OA/AA/\kappa$ coefficient is used for performance measure. However, as noted earlier, CEM is a soft detector, which contains continuous spectral information as well as BKG information under hypothesis H_0 . The measure of $OA/AA/\kappa$ cannot sufficiently take advantage of these pieces of information. Therefore, in addition to $OA/AA/\kappa$, we also introduce several objective quantitative measures, detection rate (recall rate), false alarm rate (i.e., false classification rate), precision rate, and accuracy rate to deal with the BKG issue. These rates can be calculated from a confusion matrix obtained by thresholding CEM-detection maps using Otsu's method [19].

In summary, the BSNE-ICEM presented in this paper has several contributions, which have never been explored in the past. First of all, it implements a hyperspectral subpixel target detector, CEM, to perform hyperspectral image classification, which has not been done in the past. Second, it uses BSNE to obtain nonlinear information from the data rather than using kernels to operate on the data as an SVM does. This is a new

concept that has not been investigated in hyperspectral image classification. Third, it further develops ICEM by repeatedly feeding back Gaussian-filtered CEM detection maps to gather spatial information to reprocess CEM in an iterative manner. The novelty of ICEM is introduction of an iterative feedback process to capture spatial information. No such work ever reported in the literature. Fourth, since CEM is a soft detector, Otsu's method is implemented in conjunction with CEM to make CEM a binary classifier where a confusion matrix can be constructed for performance evaluation. The use of Otsu's method is new. It converts a subpixel detection to pure-pixel classification. Finally, unlike testing samples being selected from the same class trained by training samples, such as [12], the test samples used to evaluate BSNE-ICEM are selected from all data samples, including training samples, samples from other classes and BKG samples. Since no misclassified data samples from other classes and BKG are considered for classification in [11] and [12]. To address this issue, several new objective measures from detection theory, which have never considered in hyperspectral image classification, are introduced for quantitative analysis of the hyperspectral image classification.

II. BAND SELECTION

BS is a commonly used approach and has received considerable interest lately [14]. It can be performed in a supervised or an unsupervised manner. When it is implemented as a supervised BS method, it generally specifies its application first, such as target detection, classification, endmember extraction, and spectral unmixing, which determine features for BS via prior knowledge, for example, training samples. It is then followed by a feature extraction algorithm to prioritize features to select desired bands. Consequently, the selected bands generally vary with different applications. On the other hand, when it comes to an unsupervised BS method, no prior knowledge is available to be used for BS. A general approach is to design band prioritization criteria on the basis of data characteristics or statistics, such as variance, signal-to-noise ratio, entropy, and information divergence to calculate a priority score of each of individual bands for their ranking. The bands are then selected according to their calculated priority scores. Since such BS has nothing to do with applications, the same selected bands are applied to all different applications. Regardless of whether a BS method is supervised and unsupervised uniform BS (UBS), based on our extensive experiments and reported in the literature [14], has been shown to be a reasonably good BS technique. So, in this paper, UBS is chosen for BSNE. The advantages of choosing UBS are: 1) its simplicity and easy implementation; 2) no requirement of prior knowledge or BS criteria; 3) uniform interband decorrelation, which is a best option when no prior knowledge is available according to maximum entropy in information theory; and 4) UBS allows users to select bands as sparse as possible, so that the inter-band correlation can be minimized as much as possible with a hope that the UBS-selected bands can achieve least inter-band correlation.

In this paper, we take advantage of BS to select a partial band set by UBS to avoid redundant bands being used for

classification due to highly correlated bands acquired by a hyperspectral imaging sensor. Using this small partial UBS-selected band set, we can further expand it to a large band set via nonlinear functions as described in Section III that includes nonlinear spectral information, which cannot be obtained by original full band set. Such BS coupled with nonlinear band expansion (NBE) is one of key ideas proposed in BSNE-ICEM.

III. NONLINEAR BAND DIMENSIONALITY EXPANSION

An early attempt to expand the original set of band images is to utilize nonlinear functions, for example, autocorrelation and cross correlation, an idea derived from [14] and [20]. This type of NBE process (NBEP) is referred to as correlation BE process (CBEP). Combining these new NBEP generated band images with the original set of band images provides us with sufficient band images. While NBEP may have proved to be effective to some extent, three other issues also arise. First of all, the nonlinear band images generated by CBEP may not effectively capture nonlinearity caused by other factors, such as terrain and geographical changes. To better take advantage of nonlinear spectral information among band images, a new approach, called band ratio expansion process (BREP), is further developed by finding band ratioed images, which are ratios of one band to another band for band expansion.

A. Correlation Band Expansion Process

The CBEP presented in this section is an NBE using correlation functions to generate new band images from the original set of multispectral images. Its original idea was developed in [20].

1) CBEP:

Step 1: First-order band image: $\{\mathbf{B}_l\}_{l=1}^L$ = set of original band images.

Step 2: Second-order correlated band images.

- 1) $\{\mathbf{B}_l^2\}_{l=1}^L$ = set of autocorrelated band images.
- 2) $\{\mathbf{B}_k\mathbf{B}_l\}_{k=1,l=1,k \neq l}^{L,L}$ = set of cross-correlated band images.

In case, a rescaling is needed, autocorrelated or cross-correlated band images can be normalized by the variances of band images, such as $(\sigma_{\mathbf{B}_l}^2)^{-1}\{\mathbf{B}_l^2\}$ and $(\sigma_{\mathbf{B}_k}\sigma_{\mathbf{B}_l})^{-1}\{\mathbf{B}_k\mathbf{B}_l\}$.

Step 3: Third-order correlated band images.

- 1) $\{\mathbf{B}_l^3\}_{l=1}^L$ = set of autocorrelated band images.
- 2) $\{\mathbf{B}_k^2\mathbf{B}_l\}_{k=1,l=1,l \neq k}^{L,L}$ = set of two cross-correlated band images.
- 3) $\{\mathbf{B}_k\mathbf{B}_l\mathbf{B}_m\}_{k=1,l=1,m=1,k \neq l \neq m}^{L,L,L}$ = set of three cross-correlated band images.

Similarly, like step 2, if a rescaling is needed, autocorrelated or cross-correlated band images can be normalized by the variances of band images, such as $(\sigma_{\mathbf{B}_l}^3)^{-1}\{\mathbf{B}_l^3\}$, $(\sigma_{\mathbf{B}_k}^2\sigma_{\mathbf{B}_l})^{-1}\{\mathbf{B}_k^2\mathbf{B}_l\}$, and $(\sigma_{\mathbf{B}_k}\sigma_{\mathbf{B}_l}\sigma_{\mathbf{B}_m})^{-1}\{\mathbf{B}_k\mathbf{B}_l\mathbf{B}_m\}$.

Step 4: Nonlinear correlated band images.

- 1) $\{\sqrt{\mathbf{B}_l}\}_{l=1}^L$ = set of band images stretched out by the square root.
- 2) $\{\log(\mathbf{B}_l)\}_{l=1}^L$ = set of band images stretched out by the logarithmic function.

It is worth noting that all the band images generated by NBEP are produced nonlinearly. These band images should offer useful information for data analysis, because they provide nonlinear spectral information to help to improve performance. However, we should also point out that according to our experience, using the cross-correlated band images generated by 2) in step 2 is generally sufficient to accommodate the need of NBEP. Additionally, using the set of autocorrelated band images produced by 1) in step 2 may sometimes cause nonsingularity problems in matrix computation, because they are self-correlated and usually very close to the original images. It is suggested that they should not be used alone and can be only used in conjunction with cross-correlated band images. This can be well explained by the fact that a covariance matrix, including variances and covariances, provides more information than a diagonal matrix, which only includes variances.

B. Band Ratio Expansion Process

The BREP is another NBE using different ratios of one band to another. The use of BR comes from the idea to enhance the spectral differences between bands as well as to reduce the effects of topography. It is performed by dividing one spectral band by another to produce an image that is supposed to provide relative band intensities. Such band ratioed image generally enhances the spectral differences between bands.

BR has been commonly used for multispectral data to reduce the effects caused by topological slope and aspects or to eliminate differential illumination effects caused by shadows [21], particularly, normalized difference vegetation index (NDVI) defined as the ratio of two bands to remove much of the effect of illumination in the analysis of spectral differences. For example, from a general spectral reflectance, BR with near-infrared/red (NIR/R) $\gg 1$, NIR/R < 1 , and NIR/R > 1 indicates vegetation, water, and soil, respectively. Such NIR/R-ratioed images can be used as a crude indicator in agriculture classification. Therefore, this ratio has been developed for a range of different vegetation indices. In hyperspectral data exploitation, BR was also used to detect concealed targets in hyperspectral imagery in [22].

Band ratioed images are generally obtained by dividing the pixels in one band image by the corresponding pixels in another band image to bring out differences between the spectral reflectance curves of surface types, such as the NIR/R BR.

1) Band Ratioed Expansion Process:

Step 1: Let \mathbf{B}_j and \mathbf{B}_k be the j th and k th band image vectors.

Step 2: A band image vector obtained by taking the ratio of \mathbf{B}_j to \mathbf{B}_k , denoted by \mathbf{BR}_{jk} , is defined as follows:

$$\mathbf{BR}_{jk} = \mathbf{B}_j / \mathbf{B}_k. \quad (1)$$

Assume that the gray level range for all band image vectors is given by $\{g_1, g_2, \dots, g_T\}$ in an ascending order. In case there is a pixel in \mathbf{B}_k taking gray level value 0, the gray level of the corresponding pixel in the BR image vector \mathbf{BR}_{jk} of (1) will be simply set to \mathbf{B}_j to prevent the denominator of (1)

from taking 0. As a result, the gray level range of the \mathbf{BR}_{jk} is between $1/g_T$ and g_T .

The goal of BSNE is to explore nonlinearity of data structure via NBE, which is similar to the task that a nonlinear kernel used by SVM. However, since a hyperspectral image is generally highly correlated, BS is used to select effective decorrelated bands that will be further used for NBE. UBS seems to be a good option for this purpose. That is, let the original set of hyperspectral images be denoted by $\mathbf{\Omega} = \{\mathbf{B}_l\}_{l=1}^L$. Then, BSNE combines a set of selected bands, $\{\mathbf{B}_i^{\text{BS}}\}_{i=1}^{n_{\text{BS}}}$, by BS with a new set of nonlinearly expanded bands, $\{\mathbf{B}_i^{\text{NB}}\}_{i=1}^{n_{\text{NB}}}$, to produce a new set of band images, denoted by $\mathbf{\Omega}_{\text{BSNE}} = \{\mathbf{B}_i^{\text{BS}}\}_{i=1}^{n_{\text{BS}}} \cup \{\mathbf{B}_i^{\text{NB}}\}_{i=1}^{n_{\text{NB}}}$, where n_{BS} and n_{NB} are the number of selected bands and the number of bands nonlinearly expanded from $\{\mathbf{B}_i^{\text{BS}}\}_{i=1}^{n_{\text{BS}}}$, respectively.

IV. ITERATIVE CEM

This section presents an iterative version of CEM, to be called ICEM, which is implemented in conjunction with BSNE in an iterative manner. More specifically, it utilizes BSNE to create new nonlinear band images via an NBEP. Once BSNE process is completed, a new set of hyperspectral images, $\mathbf{\Omega}_{\text{BSNE}}$, is generated. This is then followed by CEM to perform subpixel target detection in the same way that SVM is used to perform pure-pixel classification. It further feeds back its CEM-detected band images to be added to the current expanded set of band images to create another new expanded set of band images. Such feedback loop is continued on until a stopping rule is met. In order to obtain class spatial information, a Gaussian filter is introduced in the CEM-detected maps, so that spatial contextual information of data sample vectors can be captured by a Gaussian filter. The resulting Gaussian-filtered CEM-detection abundance fractional map is then fed back to create a new band image to be incorporated into $\mathbf{\Omega}_{\text{BSNE}}$ to form a new hyperspectral cube, which will be further used for reprocessing CEM again. Such repeatedly implementing CEM via feedback loops in an iterative fashion is called ICEM. For example, at each iteration, say the k th iteration, a Gaussian filter is used to blur $|\mathbf{B}|_{\text{CEM}}^{(k)}$, which is the absolute value of CEM-detection abundance fractional map, $\mathbf{B}_{\text{CEM}}^{(k)}$. This Gaussian-filtered band image, $|\mathbf{B}|_{\text{GF(CEM)}}^{(k)}$, which provides spatial classification information as similar filters used in [12], will be further fed back to $\mathbf{\Omega}_{\text{BSNE}}^{(k)}$ to create a new set of hyperspectral images, $\mathbf{\Omega}_{\text{BSNE}}^{(k+1)} = \mathbf{\Omega}_{\text{BSNE}}^{(k)} \cup \{|\mathbf{B}|_{\text{GF(CEM)}}^{(k)}\}$ for reprocessing CEM for next iteration. The same procedure is repeatedly until a stopping rule is satisfied. In order to determine a stopping rule, Otsu's method [19] is applied to $|\mathbf{B}|_{\text{GF(CEM)}}^{(k)}$ to produce a binary classification map, $\mathbf{B}_{\text{binary}}^{(k)}$, to be used to calculate Tanimoto index (TI) [23] for algorithm termination in which case $|\mathbf{B}|_{\text{CEM}}^{(k)}$ and $\mathbf{B}_{\text{binary}}^{(k)}$ will be output for final data analysis.

The detailed step-by-step implementation is provided in the following.

A. ICEM

- 1) *Initial Condition:* Let $\{\mathbf{B}_l\}_{l=1}^L$ be the original set of band images.

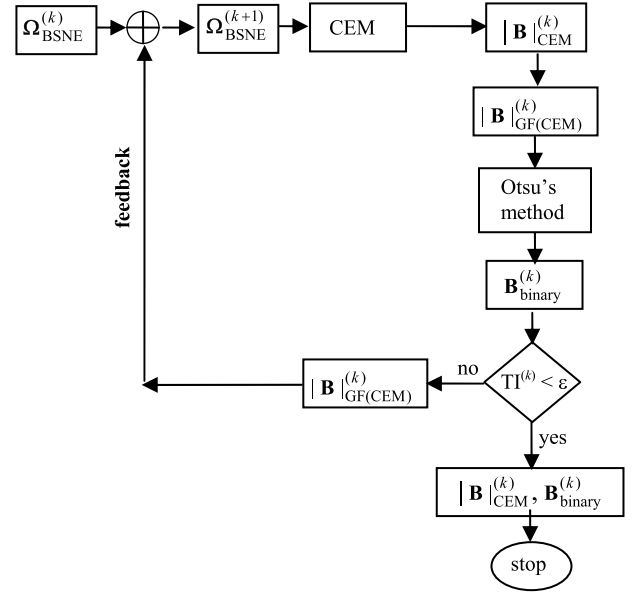


Fig. 1. Diagram of the k th iteration carried out by hyperspectral image classification implementing ICEM on $\mathbf{\Omega}_{\text{BSNE}}^{(k)}$.

- 2) Implement a BS algorithm to select a band subset $\{\mathbf{B}_l^{\text{BS}}\}_{l=1}^{n_{\text{BS}}}$.
- 3) Use an NBEP to create a new set of nonlinear band images, $\{\mathbf{B}_i^{\text{NB}}\}_{i=1}^{n_{\text{NB}}}$, where n_{NB} is the number of new band images by an NBEP.
- 4) Form a new set of band images, $\mathbf{\Omega}^{(0)} = \{\mathbf{B}_l\}_{l=1}^L \cup \{\mathbf{B}_i^{\text{NB}}\}_{i=1}^{n_{\text{NB}}}$. Let $\mathbf{d}^{(0)} = (d_1, \dots, d_L, d_1^{\text{NB}}, \dots, d_{n_{\text{NB}}}^{\text{NB}})^T$ be the desired target pixels in $\mathbf{\Omega}^{(0)}$. Let δ_0^{CEM} be CEM using $\mathbf{d}^{(0)}$ and $\mathbf{R}^{(0)}$, which are obtained from $\mathbf{\Omega}^{(0)}$. Let $k = 1$.
- 5) At the k th iteration, update $\mathbf{d}^{(k)}$ and $\mathbf{R}^{(k)} = \sum_{i=1}^N \mathbf{r}_i^{(k)} (\mathbf{r}_i^{(k)})^T$ from $\mathbf{\Omega}^{(k)}$.
- 6) Use new generated $\mathbf{d}^{(k)}$ and $\mathbf{R}^{(k)}$ for δ_k^{CEM} to be implemented on $\mathbf{\Omega}^{(k)}$. Let $\mathbf{B}_{\text{CEM}}^{(k)}$ be the detection abundance fractional map produced by δ_k^{CEM} .
- 7) Use a Gaussian filter to blur $|\mathbf{B}|_{\text{CEM}}^{(k)}$, where $|\mathbf{B}|_{\text{CEM}}^{(k)}$ is the absolute value of $\mathbf{B}_{\text{CEM}}^{(k)}$. The resulting image is denoted by Gaussian-filter $|\mathbf{B}|_{\text{GF(CEM)}}^{(k)}$.
- 8) Check if $|\mathbf{B}|_{\text{GF(CEM)}}^{(k)}$ satisfies a given stopping rule. If no, continue. Otherwise, go to step 10).
- 9) Form $\mathbf{\Omega}^{(k+1)} = \mathbf{\Omega}^{(k)} \cup \{|\mathbf{B}|_{\text{GF(CEM)}}^{(k)}\}$. Let $k \leftarrow k + 1$ and go to step 4).
- 10) $\mathbf{B}_{\text{CEM}}^{(k)}$ is the desired detection abundance fractional map and ICEM is terminated.

Fig. 1 delineates how ICEM is processed as a subpixel target detector.

V. STOPPING RULE FOR ICEM

In pattern recognition, one of popular criteria to measure segmentation/classification performance is TI defined in [23] by

$$\text{TI} = \frac{|\mathcal{S} \cap \tilde{\mathcal{S}}|}{|\mathcal{S} \cup \tilde{\mathcal{S}}|} \quad (2)$$

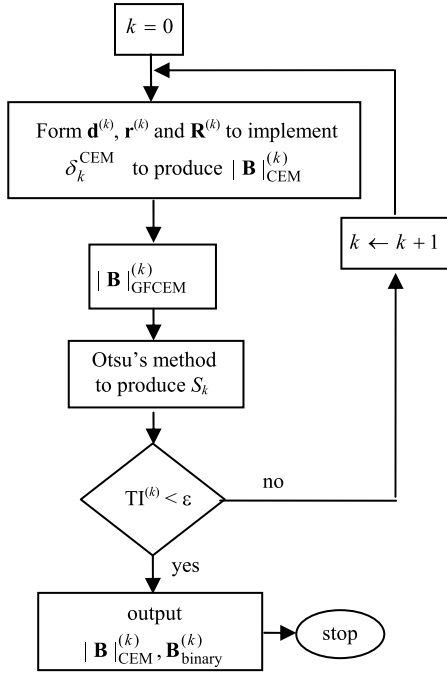


Fig. 2. Flowchart of the stopping rule used for BSNE-ICEM.

where $|A|$ is the size of a set A , S is the original image, and \tilde{S} is segmented or classified image. In other words, TI calculates a ratio of the data sample vectors in the intersection of a classified image with the original image to the union of the data sample vectors of a classified image with the original image. So, $\text{TI} = 1$ indicates that the classification rate is 1, which means that the classification is perfect so as to achieve 100% rate in the sense that all data sample vectors are classified correctly. If $\text{TI} = 0$, it indicates that the classification rate is 0, that is, the intersection of a classified image with the original image is empty, which means that no data sample vectors are classified correctly. Generally speaking, $0 \leq \text{TI} \leq 1$.

By taking advantage of TI in (2), we can use TI as a stopping rule to effectively terminate ICEM by letting, $\tilde{S} = S_k$ and $S = S_{k-1}$ be the k th thresholded binary image of the k th CEM detection abundance fractional map, $|\mathbf{B}|_{\text{CEM}}^{(k)}$, and $(k-1)$ th thresholded binary image of the $(k-1)$ th CEM detection abundance fractional map, $|\mathbf{B}|_{\text{CEM}}^{(k-1)}$. In other words, when the discrepancy between two Otsu's thresholded binary images $|\mathbf{B}|_{\text{binary}}^{(k)}$ and $|\mathbf{B}|_{\text{binary}}^{(k-1)}$ is less than ϵ , ICEM is terminated. Fig. 2 shows a flowchart of a stopping rule using TI.

VI. ALGORITHM FOR BSNE-ICEM

Using Figs. 1 and 2, an algorithm developed to implement BSNE can be described as follows.

A. BSNE-ICEM

- 1) Initial conditions are as follows.
 - a) For each class, find its sample mean to calculate the desired signature \mathbf{d} for the particular class.
 - b) Use virtual dimensionality (VD) to estimate the number of bands needed to be selected, $n_{\text{BS}} = n_{\text{VD}}$ for BSNE.

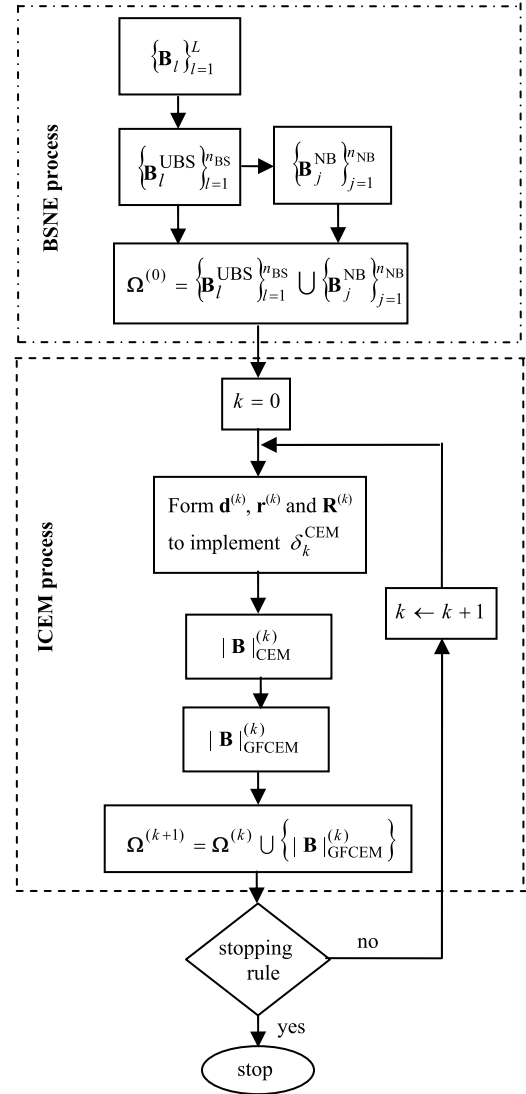


Fig. 3. Flowchart of BSNE-ICEM.

- c) Select the values of the parameter σ used for Gaussian filters in ICEM.
- d) Prescribe an error threshold ϵ for TI in (2).

- 2) Use BS to select a set of desired bands, $\{\mathbf{B}_l^{\text{BS}}\}_{l=1}^{n_{\text{BS}}}$.
- 3) Use NBEP described in Section II to generate a set of nonlinear band images, $\{\mathbf{B}_l^{\text{NB}}\}_{l=1}^{n_{\text{NB}}}$.
- 4) Apply ICEM described in Fig. 1 to $\Omega^{(0)} = \{\mathbf{B}_l^{\text{BS}}\}_{l=1}^{n_{\text{BS}}} \cup \{\mathbf{B}_l^{\text{NB}}\}_{l=1}^{n_{\text{NB}}}$.
- 5) Use TI described in Fig. 2 as a stopping rule to terminate ICEM.
- 6) Output $|\mathbf{B}|_{\text{CEM}}^{(k)}$ which is real valued and $\mathbf{B}_{\text{binary}}^{(k)}$ which is binary valued to produce a confusion matrix for classification.

Fig. 3 describes a flowchart diagram of implementing BSNE-ICEM, which has a feedback loop to update the desired signature \mathbf{d} and the sample correlation matrix \mathbf{R} from the CEM-detection abundance fractional maps iteratively. So, when both $|\mathbf{B}|_{\text{CEM}}^{(k)}$ and $|\mathbf{B}|_{\text{CEM}}^{(k-1)}$ agree within the error threshold ϵ measured by TI, ICEM is terminated.

According to Fig. 3, BSNE-ICEM has several new features that cannot be found in the current hyperspectral image classi-

fication literature including those in [1]–[13]. Since hyperspectral imagery generally has more bands than it needs, considering band expansion (BE) for hyperspectral imagery seems not practical. BSNE-ICEM shows otherwise. However, in order to show such BE to be practically useful and effective, two key elements are proposed to implement BSNE. One is BS to find effective bands to avoid two highly correlated bands to be used for BE. The other is NBEP, which expands selected bands nonlinearly via nonlinear functions where NBEP plays a similar role as a nonlinear kernel does for linear filters, such as SVM. Furthermore, ICEM makes use of Gaussian filters to smooth CEM-detection abundance fractional maps and feeds back Gaussian-filtered CEM detection abundance fractional maps to provide spatial information for reprocessing CEM iteratively by gradually increasing more spatial information through feedback loops repeatedly. Finally, the most importantly, several new quantitative measures are developed to evaluate classification performance.

VII. REAL IMAGE EXPERIMENTS

Three real hyperspectral images were used for experiments, Purdue University’s Indiana Indian Pines, University of Pavia, Italy, and Salinas, each of which has its own unique feature characteristics worth being explored. According to the recent work [12], a comprehensive comparative analysis was conducted among most existing spectral–spatial techniques, and the four edge preserving filter (EPF)-based techniques, such as EPF-B-c, EPF-G-c, EPF-B-g, and EPF-G-g, were shown to be best classification techniques where “B” and “G” are used to specify bilateral filter and guided filter, respectively, and “g” and “c” indicate that the first principal component and color composite of three principal components are used as reference images [12]. Therefore, in the following experiments, the performance of BSNE-ICEM will be evaluated in comparison with these four EPF-based techniques. Specifically, an SVM classifier was applied pixelwise with the test samples randomly selected as was done in [12] to produce class-membership maps, which were further filtered by four EPF techniques to create soft probability maps, and the maximum probability was chosen as the final class-membership. In addition to EPF-based methods, we also included experiments by the Mahalanobis distance-based maximum likelihood classification (MLC) technique [24], which was also implemented in conjunction with EPF method to capture spatial information. It should be noted that the EPF-based methods in [12] and MLC are implemented using full bands. In order to make a comprehensive analysis in comparison with BSNE-ICEM, we also performed the four EPF-based methods and MLC using BS and BSNE in exactly the same way that BSNE-ICEM was performed where BS is UBS. However, since the BSNE-MLC method suffers from singularity issue resulting from inverting the covariance matrix used in MLC, the BSNE-MLC results were not included.

As also noted in [12], the training and test samples were selected from the same class in which case misclassified sample vectors were not considered. Besides, since BKG is generally not considered in [1]–[13], the commonly performance measure, OA, which is defined as the ratio of the number of correctly classified test samples to the total number

TABLE I
CONFUSION MATRIX FOR BINARY CLASSIFICATION

detection \ true	signal	BKG
signal	TP (SD)	FP (FS)
BKG	FN (FB)	TN (BD)

of test samples, does not reflect real classification issues. To further address these problems, we also introduce several other performance measures that can measure the effects of falsely classified data sample vectors in. These measures are derived from a detection point of view based on a confusion matrix commonly used for classification.

More specifically, if we consider a particular class to be classified as a signal class of interest, then all other classes will be considered as nonsignal classes, which can be treated as a single BKG class. In this case, we can form a binary classification confusion matrix as Table I where TP, FP, FN, and TN are defined as signal detection (SD), false signal (FS) detection, false BKG (FB) detection, and BKG detection (BD), respectively.

Now, define N , N_S , and N_{BKG} as the total number of sample vectors, the total number of signal sample vectors, and BKG sample vectors where data sample vectors are divided into signal class made up of all signal sample vectors and BKG class including all nonsignal sample vectors, i.e., data sample vectors other than signal sample vectors:

N	total number of data sample vectors;
N_S	total number of signal sample vectors;
N_{BKG}	total number of BKG sample vectors;
SD	data sample vectors, which are signal sample vectors, are detected as signal sample vectors;
FS	data sample vectors, which are BKG sample vectors, are detected as signal sample vectors;
BD	data sample vectors, which are BKG sample vectors, are detected as BKG sample vectors;
FB	data sample vectors, which are signal sample vectors, are detected as BKG sample vectors;
$P_D = P_{SD}$	SD rate;
$P_F = P_{FS}$	false alarm rate/false classification rate/FS rate;
P_{BDR}	BD rate;
$P_{precision}$	precision;
$P_{accuracy}$	accuracy rate;
P_{OA}	OA rate.

According to Table I, various quantitative measures can be further defined as follows:

$$N_S = N_{SD} + N_{FB} \quad (3)$$

$$N_{BKG} = N_{BD} + N_{FS} \quad (4)$$

$$N = N_S + N_{BKG} \quad (5)$$

$$P_F = P_{FS} = \frac{N_{FS}}{N_{BD} + N_{FS}} = \frac{N_{FS}}{N_{BKG}} \quad (6)$$

TABLE II
CLASS LABELS OF 17 CLASSES

class 1 (54)	Alfalfa	class 7 (26)	grass/pasture-mowed	class 13 (212)	wheat
class 2 (1434)	corn-notill	class 8 (489)	hay-windrowed	class 14 (1294)	woods
class 3 (834)	corn-min	class 9 (20)	oats	class 15 (380)	bldg-grass green-drives
class 4 (234)	corn	class 10 (968)	soybeans-notill	class 16 (95)	stone-steel towers
class 5 (497)	grass/pasture	class 11 (2468)	soybeans-min	class 17 (10659)	BKG
class 6 (747)	grass/trees	class 12 (614)	soybeans-clean		

$$P_D = P_{SD} = \frac{N_{SD}}{N_{SD} + N_{FB}} = \frac{N_{SD}}{N_S} \quad (7)$$

$$P_{BDR} = \frac{N_{BD}}{N_{BD} + N_{FS}} = \frac{N_{BD}}{N_{BKG}} \quad (8)$$

$$P_{\text{precision}} = \frac{N_{SD}}{N_{SD} + N_{FS}} \quad (9)$$

$$P_{\text{accuracy}} = \frac{N_{SD} + N_{BD}}{N} \quad (10)$$

$$P_{OA} = \sum_{i=1}^c w(i) \frac{N_{TSD}^i}{N_{TS}^i} \text{ with } w(i) = \frac{N_{TS}^i}{\sum_{i=1}^c N_{TS}^i} \quad (11)$$

where c is the total number of classes to be classified without BKG, and N_{TSD}^i and N_{TS}^i are the numbers of test samples to be detected in class i and the number of test samples in class i . It should be noted that P_{OA} in (11) can be calculated by P_{accuracy} through

$$P_{OA} = \sum_{i=1}^c w(i) P_{\text{accuracy}}^i \text{ with } w(i) = \frac{N_{TS}^i}{\sum_{i=1}^c N_{TS}^i} \quad (12)$$

where P_{accuracy} defined in (10) can be modified as the i th class accuracy by

$$P_{\text{accuracy}}^i = \frac{N_{TSD}^i}{N_{TS}^i}. \quad (13)$$

If we further define accuracy of BKG by

$$P_{\text{accuracy}}^B = \frac{N_{BD}}{N_B} \quad (14)$$

then P_{accuracy} in (9) extended to c classes plus BKG is defined by

$$\begin{aligned} P_{\text{accuracy}} &= \sum_{i=1}^c \tilde{w}(i) P_{\text{accuracy}}^i + w(B) P_{\text{accuracy}}^B \\ &= (1 - w(B)) P_{OA} + w(B) P_{\text{accuracy}}^B \end{aligned} \quad (15)$$

where $\tilde{w}(i) = (N_{TS}^i / (\sum_{i=1}^c N_{TS}^i + N_B))$.

Since BKG was not considered as a part of classification in [12], BDR in (8) is not of interest in [12]. However, P_F in (6), P_D in (7), $P_{\text{precision}}$ in (9), and P_{accuracy} in (15) are of major interest, because they are involved with the number of falsely misclassified data samples, N_{FS} , which is not considered in P_{OA} in [12, eqs. (11) and (12)].

The test samples used in the following comparative EPF-based experiments were entire pixels in the data to be processed. In this case, training samples and BKG pixels were also included as test samples. As a result, the evaluation was performed quite different from that carried out in [12] where only the training and test samples from the same class were

used for evaluation and BKG was not considered as a class but rather excluded from classification.

A. Purdue Indiana Indian Pines

A real image used for experiments is a well-known Airborne Visible Infrared Imaging Spectrometer (AVIRIS) image scene, Purdue Indiana Indian Pines test site shown in Fig. 4(a), its ground truth in Fig. 4(b) along with its 17 class maps in Fig. 4(d), and aerial view in Fig. 4(c). Table II also tabulates all the specific types of 16 classes. It has a size of 145×145 pixel vectors taken from an area of mixed agriculture and forestry in Northwestern Indiana, USA, with details of band and wavelength is given in caption. The data set is available at website <http://cobweb.ecn.purdue.edu/~biehl/MultiSpec/documentation.html>. It was recorded in June 1992 with 220 bands, which include water absorption bands (bands 104–108 and 150–162). For our experiments, these water bands were removed.

In order to implement BSNE, we first determine how many bands needed to be selected, n_{BS} , where VD developed in [18] and [25] was used to estimate the value of n_{BS} , which is 29 [14]. In this case, a simple BS method, UBS, was used to select $\{\mathbf{B}_l^{\text{UBS}}\}_{l=1}^{29}$. Since the wavelength range is across visible and infrared wavelengths, we used BREP instead of CBEP to expand new nonlinear bands from $\{\mathbf{B}_l^{\text{UBS}}\}_{l=1}^{29}$ to generate $2 \binom{29}{2} = 812$ band ratioed bands, $\{\mathbf{B}_l^{\text{BREP}}\}_{l=1}^{812}$. That is, according to (1) for every pair $(\mathbf{B}_j, \mathbf{B}_k)$, we can have two band ratioed images, $\mathbf{BR}_{jk} = \mathbf{B}_j / \mathbf{B}_k$ and $\mathbf{BR}_{kj} = \mathbf{B}_k / \mathbf{B}_j$. As a result, a total of 812 bands, $\mathbf{\Omega}^{(0)} = \{\mathbf{B}_l^{\text{UBS}}\}_{l=1}^{29} \cup \{\mathbf{B}_l^{\text{BREP}}\}_{l=1}^{812}$, was used for ICEM. Table III tabulates the specifications of parameters and various methods used by BSNE-ICEM. Fig. 5 shows 16 ICEM-detection real-valued class maps obtained from using $\mathbf{\Omega}^{(0)}$, and Fig. 6 shows their binary maps obtained by applying Otsu's thresholding method to the real-valued class maps in Fig. 5.

According to the ground truth in Table II, each of corn, soybean, and grass has three different types. In this case, 16 classes are divided into 4 subclasses, corn-like classes 2–4, grass-like classes 5–7, soybean-like classes 10–12, and other remaining classes plus BKG class 17. Fig. 7 shows the spectral profiles of these 4 classes plotted by 16 class means where the spectral signatures of three corn classes are very close each other and so are the three soybean classes. As expected, classifying these classes will be very challenging.

Table IV tabulates results produced by BSNE-ICEM, EPF-B-g, EPF-B-c, EPF-G-g, and EPF-G-c using five performance measures, P_D in (7), P_F in (6), $P_{\text{precision}}$ in (9), P_{OA} in (11) and (12), and P_{accuracy} in (15) in terms of percentile (%)

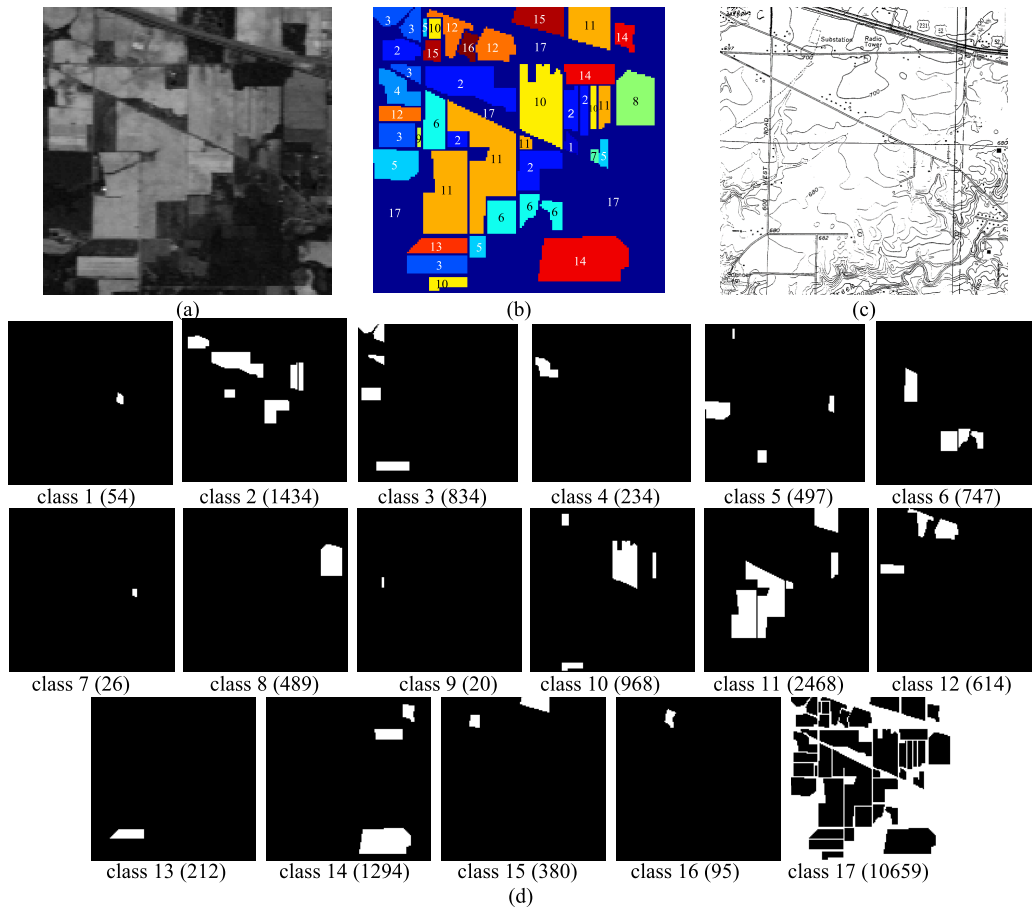


Fig. 4. Purdue Indiana Indian Pines scene. (a) Band 186 (2162.56 nm). (b) Ground-truth map. (c) USGS Quadrangle map of the test site. (d) 17 class maps.

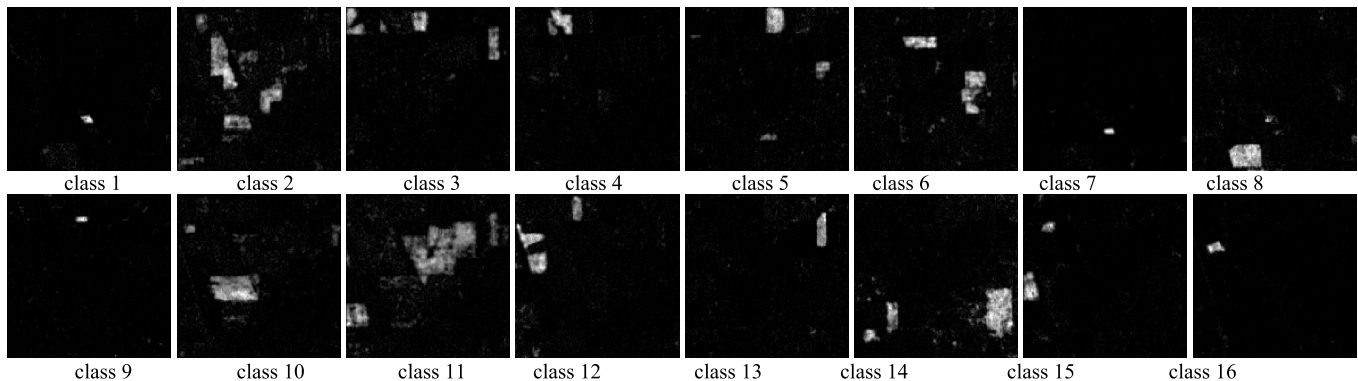


Fig. 5. 16 ICEM-detection abundance fractional class maps from original bands expanded by band ratioed bands (812 bands) from uniformly selected 29 bands.

where $P_D\%$, $P_F\%$, and $P_{\text{precision}}$ are shown in the three columns under each method, and P_{OA} and P_{accuracy} are shown in the last two rows with the bold faced values indicating the best results. It should be noted that according to the codes provided in [12] the obtained results are fluctuated and not necessarily consistent with the results in [12].

According to Table IV, the best P_{OA} was the one produced by EPF-B-c, while the best accuracy was produced by BSNE-ICEM using Otsu's thresholding. As for the other three performance measures, P_D , P_F , and $P_{\text{precision}}$, EPF-G-c generally produced the best P_D values for 8 out of 16 classes, and BSNE-ICEM produced the best values of P_F and $P_{\text{precision}}$

almost across board except class 9 whose best values of P_F and $P_{\text{precision}}$ were produced by EPF-G-c. The most interesting finding is P_{accuracy} defined in (15), which includes BKG classification into P_{OA} in (11) and (12). As shown in the last row of Table IV, BSNE-ICEM produced nearly twice better P_{accuracy} than four EPF-based methods, which did not include BKG classification in their results in [12]. It is known that P_{OA} is the major performance measure which has been widely used to evaluate hyperspectral image classification [1]–[12]. Unfortunately, P_{OA} only tells half of a story, which is that it does not account for BKG classification, but rather calculates the correct classification of test data samples where

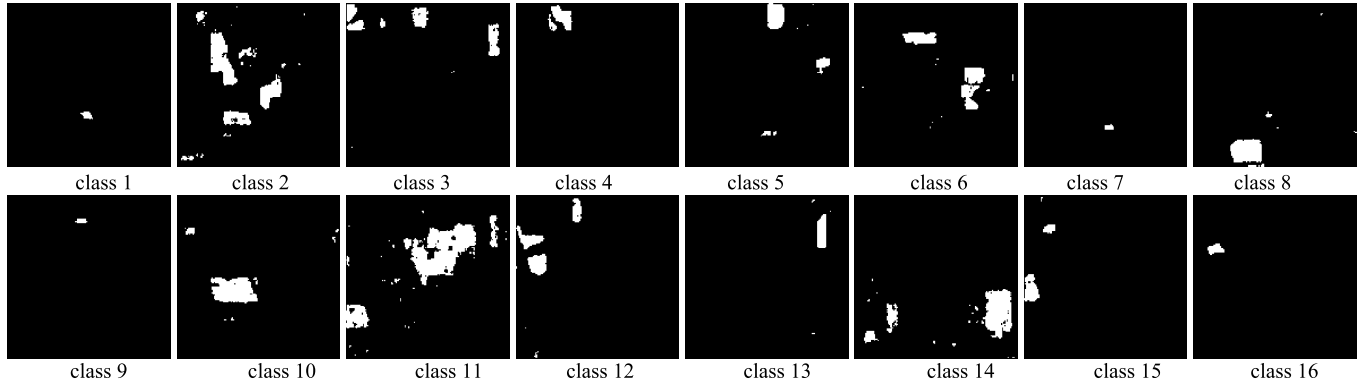


Fig. 6. 16 BSNE-ICEM detection abundance fractional class maps in Fig. 5 thresholded by Otsu's method.

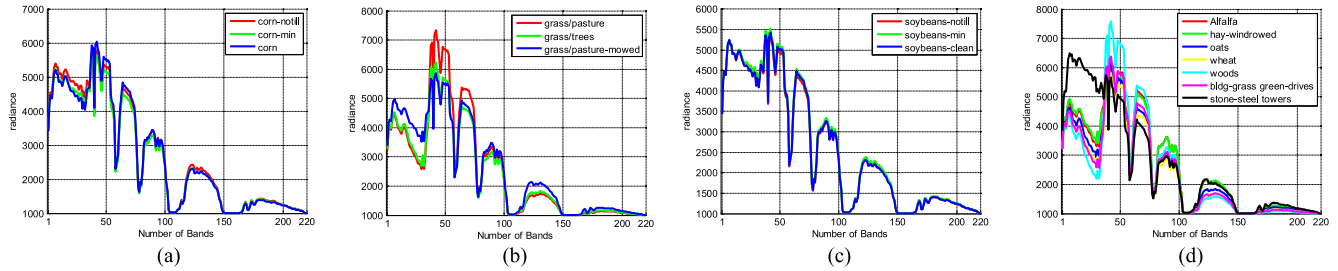


Fig. 7. Spectral profiles of 16 class sample means in Purdue Indian Pines. (a) Corn classes. (b) Grass classes. (c) Soybean classes. (d) Other classes.

TABLE III
SPECIFICATIONS OF PARAMETERS USED BY BSNE-ICEM FOR THE PURDUE INDIAN PINES SCENE

Band selection method	UBS (29 bands)															
Nonlinear expanded bands	BREP (812 bands)															
d	Class sample mean															
Class #	1	2	3	4	5	6	7	8	9	10	11	12	13	14	15	16
Iteration #	3	3	3	3	3	3	6	3	6	3	4	3	6	3	3	10
Gaussian window size	11 × 11															
σ used in Gaussian filter	0.5 with window size 11 × 11															
Thresholding method	Otsu's method															
stopping threshold (TI)	0.85															

TABLE IV
PERFORMANCE EVALUATION COMPARISON AMONG BSNE-ICEM AND FOUR EPF-BASED METHODS, EPF-B-g, EPF-B-c, EPF-G-g, and EPF-G-c FOR THE INDIAN PINES SCENE

Class	BSNE-ICEM			EPF-B-g			EPF-B-c			EPF-G-g			EPF-G-c		
	P _D %	P _F %	P _{precision} %	P _D %	P _F %	P _{precision} %	P _D %	P _F %	P _{precision} %	P _D %	P _F %	P _{precision} %	P _D %	P _F %	P _{precision} %
1	74.55	0.02	89.13	100.00	0.16	57.50	97.83	0.16	57.69	97.83	0.15	58.44	100.00	0.14	60.53
2	79.71	1.14	83.48	85.01	3.11	67.03	84.94	3.12	66.91	85.22	3.11	67.09	84.45	3.27	65.76
3	64.53	0.14	95.76	93.13	1.33	74.40	94.10	1.41	73.54	92.41	1.41	73.12	92.41	1.34	74.11
4	95.80	0.28	79.72	99.16	0.62	64.74	99.16	0.62	64.56	99.16	0.75	60.26	99.16	0.76	59.95
5	86.75	0.17	92.09	93.58	3.46	39.65	93.37	3.20	41.45	94.00	3.11	42.23	93.58	2.93	43.55
6	90.41	0.27	92.18	100.00	3.88	49.06	99.73	3.89	48.92	99.73	4.25	46.82	100.00	3.94	48.70
7	96.55	0.04	77.78	96.43	0.08	62.79	96.43	0.07	65.85	96.43	0.10	56.25	96.43	0.10	56.25
8	99.37	0.36	86.36	100.00	1.01	69.88	100.00	0.99	70.40	100.00	0.92	71.77	100.00	0.94	71.34
9	90.00	0.08	52.94	95.00	0.14	38.78	100.00	0.13	42.55	100.00	0.08	55.56	95.00	0.05	63.33
10	75.00	0.27	93.06	82.30	2.41	62.70	82.82	2.50	61.97	81.79	2.45	62.21	82.51	2.44	62.51
11	75.89	1.43	87.48	95.23	3.95	76.71	95.64	3.99	76.63	94.46	3.84	77.02	94.70	3.76	77.45
12	92.24	0.28	90.41	98.82	1.75	62.47	98.65	1.68	63.38	98.48	1.81	61.67	98.65	1.85	61.13
13	99.02	0.10	90.22	99.02	0.25	79.61	99.02	0.29	77.19	99.51	0.30	76.69	99.51	0.36	73.12
14	83.24	0.32	94.19	98.26	15.48	31.91	98.50	15.80	31.58	98.10	15.46	31.90	98.50	15.48	31.97
15	77.20	0.02	98.35	96.63	26.91	7.85	96.89	26.59	7.94	94.30	26.91	7.67	99.48	27.28	7.99
16	98.92	0.02	94.85	96.77	0.35	54.88	98.92	0.32	57.86	100.00	0.41	52.25	100.00	0.40	52.54
P _{OA}	80.89			94.83			95.33			94.99			94.60		
P _{accuracy}	87.54			46.23			46.47			46.31			46.12		

both training samples and testing samples come from the same class. That is, P_{OA} does not include misclassification of data samples from other classes such as BKG class. To be more specific, if we consider multiclass confusion matrix, P_{OA} only calculates the correct classification rates

for all classes along the diagonal line without BKG, while discarding all misclassification rates off diagonal line. Such misclassification rates are exactly the other half story must be told in accuracy calculation. However, how to address misclassification rates is challenging, because there are

TABLE V
PERFORMANCE EVALUATION COMPARISON AMONG BS-SVM-EPF-BASED METHODS FOR THE INDIAN PINES SCENE

Class	BS-SVM-EPF-B-g			BS-SVM-EPF-B-c			BS-SVM-EPF-G-g			BS-SVM-EPF-G-c		
	$P_D\%$	$P_F\%$	$P_{\text{precision}}\%$									
1	100.00	0.19	53.49	97.83	0.19	53.57	100.00	0.19	54.12	100.00	0.33	40.00
2	81.09	2.94	66.74	81.09	4.22	58.34	84.80	2.95	67.69	91.67	3.66	64.61
3	90.12	2.99	55.37	70.72	1.65	63.80	91.81	3.91	49.13	81.08	2.09	61.46
4	99.16	0.70	61.84	99.16	1.56	41.96	100.00	1.39	45.06	100.00	2.75	29.33
5	94.62	4.48	33.16	95.24	7.70	22.53	97.72	7.92	22.50	96.48	6.71	25.27
6	98.63	4.60	43.53	99.45	3.02	54.22	98.36	6.06	36.86	99.73	5.93	37.68
7	96.43	0.11	52.94	92.86	0.05	72.22	96.43	0.16	45.00	96.43	0.12	51.92
8	100.0	0.97	70.50	100.0	0.96	70.71	100.00	0.91	71.99	100.00	0.78	74.80
9	90.00	0.11	43.90	100.0	0.20	32.79	100.00	0.13	42.55	40.00	0.01	80.00
10	85.19	2.53	61.98	85.60	2.79	59.77	89.09	2.30	65.26	90.23	2.63	62.42
11	85.17	3.44	76.59	86.23	3.44	76.84	87.05	3.27	77.85	86.60	3.24	77.96
12	99.16	2.31	55.52	91.40	2.29	53.72	92.41	1.51	64.02	97.47	1.14	71.27
13	99.02	0.32	75.46	99.51	0.35	73.91	99.51	0.45	68.69	100.00	0.73	57.42
14	98.81	13.96	31.19	95.49	12.94	32.08	95.02	12.24	33.20	90.67	9.90	36.96
15	92.49	18.08	8.73	100.0	17.02	9.90	95.85	13.71	11.56	96.89	16.89	9.69
16	98.92	0.43	50.83	98.92	0.64	40.71	100.00	0.56	44.08	98.92	0.72	38.02
P_{OA}	90.70			88.95			91.63			91.43		
P_{accuracy}	44.21			43.36			44.67			44.57		

$\binom{c}{2} = ((c-1))/2$ combinations of misclassification rates, where c is the total number of classes, which can be referred to as one against one strategy. An alternative strategy is one against rest, which considers a class of interest as the desired class and all the rest of classes including BKG class as the BKG. By doing so, a multiclass confusion matrix is further simplified to a binary confusion matrix in which case a standard binary hypothesis testing problem can be applied. With this interpretation, we can include the BKG class, class 17 as a new class, a case not considered in [12]. In other words, we can consider the class of interest as signal class specified by the alternative hypothesis H_1 and the BKG as the null hypothesis H_0 . Then, P_D is calculated by the correct classification rate of samples from the signal class whereas P_F is the false alarm rate defined as the rate of misclassifying the samples from BKG into the signal class. Such misclassified data samples are referred to falsely alarmed or falsely classified data samples. The measures of P_F in (6), $P_{\text{precision}}$ in (9), and P_{accuracy} in (15) are particularly designed to address this issue. By virtue of these five performance measures calculated in Table IV, BSNE-ICEM was the best to produce the best values of P_F , $P_{\text{precision}}$, and P_{accuracy} , while EPF-G-c and EPF-B-c were the best to produce the best values of P_D and P_{OA} , respectively. As also noted, BSNE-ICEM had a lower detection accuracy but a higher classification accuracy. This is mainly due to the fact that the detection rate is calculated by the detection of a target of interest from all data sample vectors including BKG class. It is quite different from EPF-based methods, which only calculated detection rates of targets from the same class that has been used for training. Most importantly, if we examine the spectral signature profiles of four categories of 16 classes, their respective signatures are very similar and close. This indicates that the classification among these classes cannot be too high as shown by P_{OA} in the second row from the last in Table III, which was around 95%. Instead, $P_{\text{precision}}$ tabulated in the third column under each of four EPF-based methods did reflect the difficulty of classifying each of these classes. P_{accuracy} tabulated in the last row in Table III indeed

provided evidence the overall classification difficulty, which was around 46% produced by the four EPF-based methods and 87.54% produced by BSNE-ICEM. This implies that $P_{\text{precision}}$ and P_{accuracy} should be the ones to be used to measure class classification difficulty not P_{OA} . So, generally speaking, BSNE-ICEM is the best classification technique to deal with correct classification and misclassification issues.

In order to see how BS and BSNE affect EPF-based methods, we also implemented four EPF-based methods using the same bands selected by BSNE that were used by BSNE-ICEM; Tables V and VI tabulate their results, which were not as good as the results in Table IV. This demonstrated that when the pure-pixel-based spectral classifier, such as SVM, is used for classification, full band information provides better performance than partial bands. Although BSNE using partial bands with NBE performed better than BS without NBE, its included nonlinear spectral information was insufficient to compete EPF-based methods using full bands. Similar conclusions were also drawn from MLC, which is also a pure-pixel-based spectral classifier where Tables VII and VIII tabulate their results without BS and with BS, respectively. Also comparing Tables IV–VI with Tables VII and VIII, it clearly shows that the EPF-based methods performed significantly better than MLC.

B. Salinas

The Salinas image shown in Fig. 8(a) was acquired by the AVIRIS sensor over Salinas Valley, CA, and with a spatial resolution of 3.7 m per pixel with a spectral resolution of 10 nm. The image has a size of $512 \times 217 \times 224$. Fig. 8(b) and (c) shows the color composite of the Salinas image and the corresponding ground-truth class labels. The VD estimated for this scene was 21 for UBS to select 21 bands. Since this scene is very similar to the Purdue Indiana Indian Pines scene, which also includes 20 water absorption bands, which are 108–112, 154–167, and 224, only BREP was used for NBE, $\{\mathbf{B}_l^{\text{BREP}}\}_{l=1}^{420}$. Table IX tabulates the specifications of parameters

TABLE VI
PERFORMANCE EVALUATION COMPARISON AMONG BSNE-SVM-EPF-BASED METHODS FOR THE INDIAN PINES SCENE

Class	BSNE-SVM-EPF-B-g			BSNE-SVM-EPF-B-c			BSNE-SVM-EPF-G-g			BSNE-SVM-EPF-G-c		
	P _D %	P _F %	P _{precision} %	P _D %	P _F %	P _{precision} %	P _D %	P _F %	P _{precision} %	P _D %	P _F %	P _{precision} %
1	100.00	0.11	65.71	100.00	0.10	67.65	100.00	0.09	70.77	100.00	0.09	71.88
2	84.38	1.88	76.56	87.68	1.97	76.43	70.17	1.37	78.90	65.90	1.74	73.40
3	92.41	1.30	74.54	88.67	1.81	66.79	77.35	0.91	77.82	84.10	1.11	75.70
4	99.58	1.17	49.27	99.58	1.02	52.80	100.00	0.91	55.63	99.58	1.06	51.64
5	91.93	1.54	58.34	87.99	1.43	59.11	94.41	1.37	61.79	94.20	1.33	62.50
6	99.73	3.66	49.49	99.45	1.87	65.70	98.22	1.90	65.00	99.86	2.75	56.64
7	96.43	0.04	77.14	92.86	0.01	89.66	96.43	0.03	79.41	96.43	0.03	79.41
8	100.00	0.75	75.51	99.58	0.78	74.73	99.79	0.66	77.94	100.00	0.66	77.85
9	0.00	0.00	0.00	5.00	0.00	100.00	30.00	0.00	100.00	0.00	0.00	0.00
10	95.99	2.13	68.60	95.78	2.47	65.24	93.00	2.15	67.72	96.71	2.89	61.88
11	94.75	3.32	79.06	93.40	3.20	79.43	97.64	7.25	64.04	88.35	4.20	73.55
12	96.46	1.09	72.04	97.64	1.05	73.01	95.95	1.05	72.58	98.65	2.27	55.82
13	98.54	0.12	88.60	99.02	0.22	81.85	99.51	0.16	86.08	99.51	0.18	84.65
14	97.94	10.94	36.43	97.00	8.70	41.64	93.99	9.31	39.27	94.39	9.47	38.96
15	96.63	27.90	6.08	100.00	31.37	5.63	100.00	30.52	5.77	100.00	30.62	5.76
16	98.92	0.11	79.31	98.92	0.11	79.31	100.00	0.20	69.40	95.70	0.10	80.91
P _{OA}	94.33			94.01			91.25			89.54		
P _{accuracy}	45.98			45.83			44.48			43.65		

TABLE VII
PERFORMANCE EVALUATION COMPARISON AMONG MLC-EPF-BASED METHODS FOR THE INDIAN PINES SCENE

Class	MLC-EPF-B-g			MLC-EPF-B-c			MLC-EPF-G-g			MLC-EPF-G-c		
	P _D %	P _F %	P _{precision} %	P _D %	P _F %	P _{precision} %	P _D %	P _F %	P _{precision} %	P _D %	P _F %	P _{precision} %
1	100.00	0.15	58.97	93.48	0.14	59.72	97.83	0.13	62.50	100.00	0.12	63.89
2	92.51	4.43	60.35	93.00	4.20	61.74	91.95	4.27	61.07	91.88	4.00	62.63
3	71.81	3.15	48.34	72.53	3.24	47.89	72.53	3.28	47.63	71.69	3.08	48.89
4	100.00	0.96	54.23	100.00	0.91	55.63	100.00	0.95	54.61	99.58	0.90	55.66
5	65.84	2.36	39.60	65.84	2.35	39.70	65.84	2.42	38.97	65.84	2.33	39.90
6	100.00	6.51	35.58	100.00	6.43	35.87	100.00	6.52	35.54	100.00	6.46	35.77
7	100.00	0.17	44.44	100.00	0.14	49.12	100.00	0.13	50.00	100.00	0.09	59.57
8	100.00	1.57	59.75	100.00	1.74	57.25	100.00	1.47	61.20	100.00	1.35	63.23
9	100.00	0.08	54.05	95.00	0.05	65.52	95.00	0.07	57.58	85.00	0.03	73.91
10	98.35	4.94	49.10	98.05	4.89	49.30	98.05	4.89	49.30	97.74	4.91	49.12
11	73.65	5.47	64.02	73.56	5.35	64.52	73.97	5.27	64.97	76.05	5.07	66.46
12	81.79	3.93	37.66	82.46	3.78	38.78	83.47	3.74	39.29	82.29	4.06	37.03
13	100.00	0.63	61.01	100.00	0.62	61.19	99.51	0.61	61.82	99.51	0.60	62.20
14	90.43	14.97	27.88	90.36	15.38	27.32	90.43	15.09	27.73	90.43	15.54	27.14
15	99.48	11.13	14.32	100.00	11.22	14.29	100.00	11.49	14.00	99.22	11.66	13.73
16	98.92	0.29	60.13	98.92	0.27	61.74	98.92	0.34	56.10	92.47	0.35	53.75
P _{OA}	86.33			86.42			86.45			86.66		
P _{accuracy}	42.08			42.13			42.14			42.24		

TABLE VIII
PERFORMANCE EVALUATION COMPARISON AMONG BS-MLC-EPF-BASED METHODS FOR THE INDIAN PINES SCENE

Class	BS-MLC-EPF-B-g			BS-MLC-EPF-B-c			BS-MLC-EPF-G-g			BS-MLC-EPF-G-c		
	P _D %	P _F %	P _{precision} %	P _D %	P _F %	P _{precision} %	P _D %	P _F %	P _{precision} %	P _D %	P _F %	P _{precision} %
1	97.83	0.14	60.81	93.48	0.13	60.56	97.83	0.12	63.38	100.00	0.11	65.71
2	85.99	4.11	60.37	86.20	4.18	60.02	84.31	4.13	59.81	82.07	4.22	58.63
3	46.39	1.58	54.69	46.99	1.57	55.16	47.35	1.69	53.54	46.14	1.69	52.90
4	97.89	1.22	47.74	100.00	1.21	48.47	91.98	1.15	47.70	87.76	1.20	45.51
5	65.01	2.40	38.96	65.63	2.46	38.52	65.22	2.51	37.95	65.42	2.54	37.75
6	100.00	7.55	32.26	100.00	7.46	32.55	100.00	7.69	31.88	100.00	7.50	32.42
7	100.00	0.24	35.90	100.00	0.24	35.44	100.00	0.22	37.33	100.00	0.20	40.58
8	100.00	1.82	56.10	100.00	1.89	55.13	100.00	1.71	57.66	100.00	1.60	59.23
9	90.00	0.26	24.66	75.00	0.08	46.88	100.00	0.29	24.69	90.00	0.22	27.69
10	82.00	6.14	39.30	78.09	6.15	38.10	77.67	6.25	37.60	75.62	6.34	36.62
11	50.22	2.92	69.46	50.31	2.97	69.11	49.82	2.82	70.05	50.31	3.10	68.19
12	76.39	6.40	25.72	76.22	6.48	25.46	76.22	6.25	26.14	75.72	6.06	26.60
13	100.00	1.26	43.90	100.00	1.20	45.15	100.00	1.28	43.43	100.00	1.17	45.76
14	90.91	14.05	29.28	90.59	14.32	28.83	90.67	14.21	29.01	90.28	14.47	28.54
15	92.75	15.18	10.26	95.85	15.12	10.60	93.52	15.26	10.28	95.60	15.49	10.35
16	97.85	0.55	43.96	98.92	0.46	48.68	98.92	0.64	40.89	96.77	0.64	40.18
P _{OA}	75.57			75.40			74.80			74.19		
P _{accuracy}	36.84			36.76			36.46			36.17		

and various methods used by BSNE-ICEM. Fig. 9 shows 16 ICEM-detection real-valued class maps obtained from using $\Omega^{(0)} = \{\mathbf{B}_l^{UBS}\}_{l=1}^{21} \cup \{\mathbf{B}_l^{BREP}\}_{l=1}^{420}$, and Fig. 10 shows their binary maps obtained by applying Otsu’s thresholding method to the real-valued class maps in Fig. 9. According to the ground truth

in Fig. 8(b), 16 classes are divided into 5 subclasses, weeds classes 1 and 2, fallow classes 3–5, lettuce classes 11–14, vineyard classes 15 and 16, and other remaining classes plus BKG class = 0. Fig. 11 shows the spectral profiles of these 5 classes plotted by 16 class means.

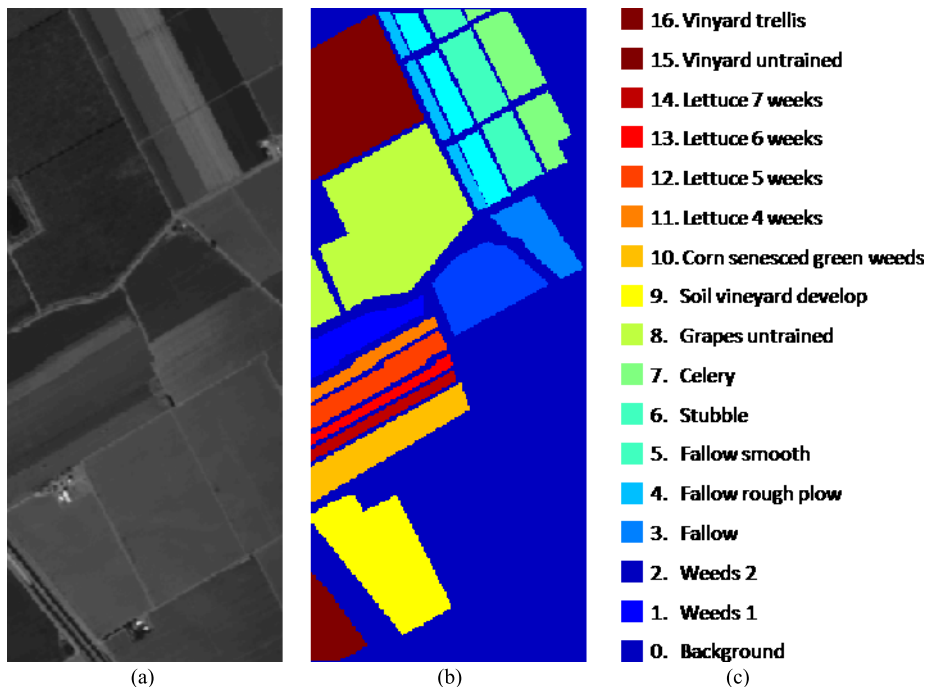


Fig. 8. Ground truth of the Salinas scene with 16 classes. (a) Salinas scene. (b) Color ground-truth image. (c) Ground-truth class labels.

TABLE IX
SPECIFICATIONS OF PARAMETERS USED BY BSNE-ICEM FOR THE SALINAS SCENE

Band selection method	UBS (21)															
Nonlinear expanded bands	BREP (420)															
d	Class sample mean															
Class #	1	2	3	4	5	6	7	8	9	10	11	12	13	14	15	16
Iteration #	2	5	4	4	3	3	3	6	3	5	4	3	5	4	9	2
Gaussian window size	11×11															
σ used in Gaussian filter	0.7 with window size 11×11															
Thresholding method	Otsu's method															
stopping threshold (TI)	0.97															

As discussed in the Purdue Indian Pines data experiments, we also used one against rest to calculate the five performance measures, P_D in (7), P_F in (6), $P_{\text{precision}}$ in (9), P_{accuracy} in (15), and P_{OA} in (11) and (12) where BKG class, class 0, is also included for classification. Table X tabulates the results produced by BSNE-ICEM, EPF-B-g, EPF-B-c, EPF-G-g, and EPF-G-c using five performance measures, P_D in (7), P_F in (6), $P_{\text{precision}}$ in (9), P_{OA} in (11) and (12), and P_{accuracy} in (15) in terms of percentile (%) where $P_D\%$, $P_F\%$, and $P_{\text{precision}}$ are shown in the three columns under each method, and P_{OA} and P_{accuracy} are shown in the last two rows with the bold faced values indicating the best results.

According to Table X, the results obtained from the Salinas scene were very similar and close to the results in Table IV for the Purdue Indian Pines scene. So, similar conclusions drawn from the Purdue Indian Pines scene can also be applied to the Salinas scene. That is, the best P_{OA} was the one produced by EPF-G-c, while the best P_{accuracy} was produced by BSNE-ICEM. As for the other three performance measures, P_D , P_F , and $P_{\text{precision}}$, EPF-G-c generally produced the best P_D values for 14 out of 16 classes, and BSNE-ICEM produced

the best values of P_F and $P_{\text{precision}}$ almost across board except class 8 whose best values of P_F and $P_{\text{precision}}$ were produced by EPF-G-c. In analogy with the Purdue Indian Pines scene, BSNE-ICEM was the best to produce the best values of P_F , $P_{\text{precision}}$, and P_{accuracy} . This also concludes that BSNE-ICEM is generally the best classification technique to deal with correct and classification and misclassification issues.

Like the Purdue Indian Pines scene, we also performed experiments for the Salinas scene and implemented four EPF-based methods and MLC using the same bands selected by BS and BSNE that were used by BSNE-ICEM for the Salinas scene. Tables XI–XIV tabulate their respective results, which were also not as good as the results in Table X. The same conclusions drawn for the Purdue Indian Pines scene were also applied to the Salinas scene.

C. University of Pavia

The University of Pavia image, which includes an urban area surrounding the University of Pavia, Italy, was collected by the ROSIS-03 satellite sensor. It is of size $610 \times 340 \times 115$

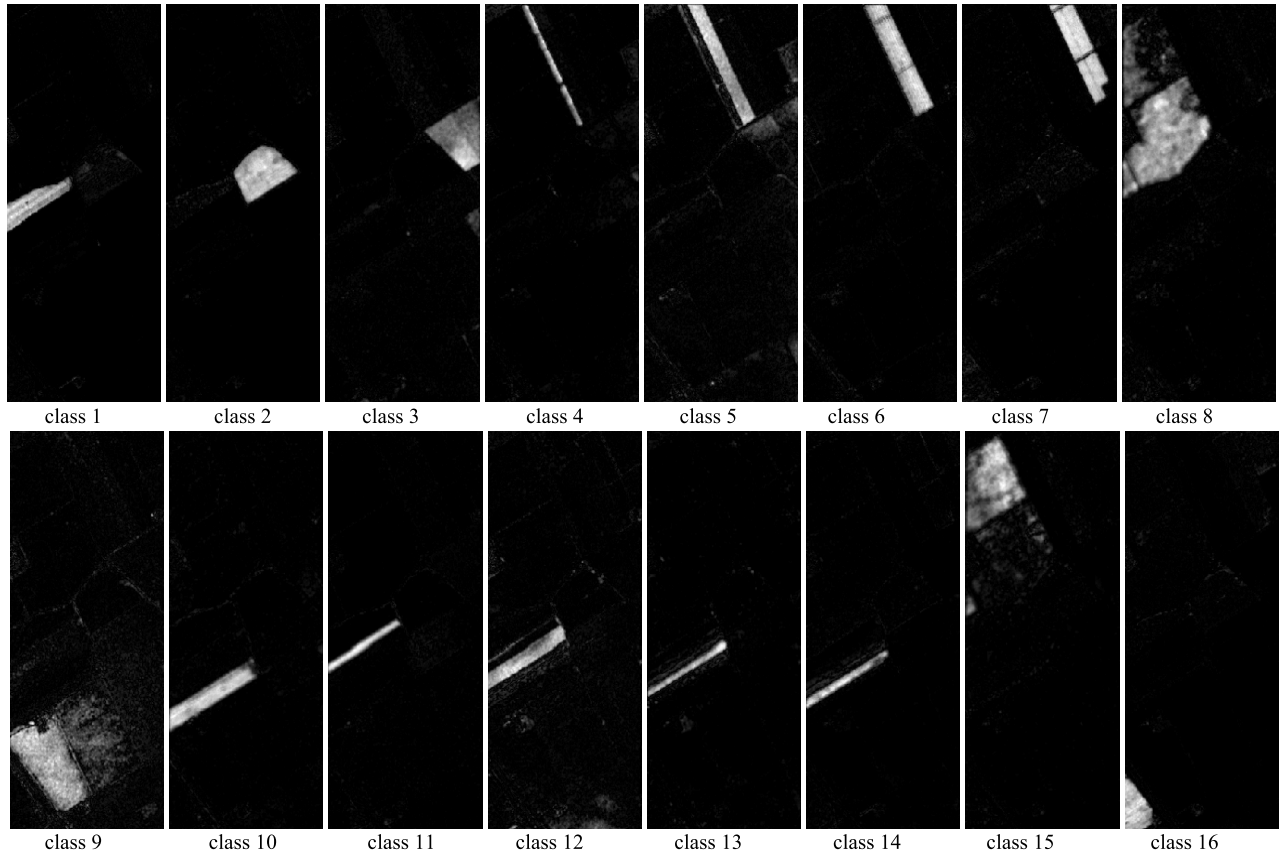


Fig. 9. ICEM 16 detection abundance fractional class maps from original bands expanded from uniformly selected 21 bands by band ratioed bands (420 bands) for the Salinas scene.

TABLE X
PERFORMANCE EVALUATION COMPARISON AMONG BSNE-ICEM AND FOUR EPF-BASED METHODS, EPF-B-c, EPF-B-g, EPF-G-c, and EPF-G-g FOR THE SALINAS SCENE

Class	BSNE-ICEM			EPF-B-g			EPF-B-c			EPF-G-g			EPF-G-c		
	P _D %	P _F %	P _{precision} %	P _D %	P _F %	P _{precision} %	P _D %	P _F %	P _{precision} %	P _D %	P _F %	P _{precision} %	P _D %	P _F %	P _{precision} %
1	99.90	0.31	85.51	100.00	0.68	73.19	100.00	0.65	74.05	100.00	0.65	74.00	100.00	0.75	71.22
2	97.50	0.07	97.87	100.00	2.78	56.22	99.97	2.78	56.21	100.00	2.72	56.72	100.00	2.96	54.67
3	97.82	1.89	49.09	100.00	14.99	12.20	100.00	14.95	12.22	100.00	15.09	12.13	100.00	15.14	12.10
4	83.43	0.06	94.17	100.00	4.41	23.13	100.00	4.38	23.25	100.00	4.43	23.04	100.00	4.54	22.64
5	97.84	0.69	77.77	98.51	1.95	55.95	98.36	1.97	55.66	98.47	1.92	56.29	98.84	1.83	57.61
6	98.08	0.32	91.86	100.00	0.83	81.75	100.00	0.86	81.18	100.00	0.84	81.58	100.00	0.89	80.65
7	97.18	0.17	95.08	100.00	0.87	79.34	100.00	0.83	80.14	100.00	0.83	80.21	99.97	0.87	79.48
8	84.54	1.67	85.14	81.52	1.35	87.11	81.47	1.38	86.84	82.37	1.22	88.33	83.52	1.18	88.82
9	95.78	2.06	73.49	99.85	12.16	35.25	99.84	12.11	35.33	99.87	12.20	35.19	99.87	12.38	34.90
10	88.02	0.07	97.47	96.19	8.10	28.06	96.06	8.21	27.77	96.49	8.17	27.96	97.86	7.40	30.16
11	92.51	0.10	89.49	100.00	3.25	23.57	99.91	3.24	23.58	100.00	3.22	23.71	100.00	3.15	24.09
12	96.32	0.61	73.39	100.00	4.90	27.42	100.00	4.92	27.36	100.00	4.96	27.20	100.00	4.95	27.23
13	91.60	0.22	77.49	99.13	0.40	67.16	99.45	0.40	67.38	99.56	0.41	66.91	99.78	0.42	66.52
14	88.24	0.26	76.27	100.00	0.50	65.97	100.00	0.51	65.64	100.00	0.52	65.40	100.00	0.46	67.85
15	67.37	0.30	94.54	93.82	2.09	76.17	93.26	2.11	75.86	94.32	2.02	76.86	96.19	1.94	77.94
16	96.40	0.14	91.97	99.61	0.73	69.47	99.56	0.74	69.19	99.39	0.70	70.35	99.67	0.70	70.38
P _{OA}	88.93			95.87			95.70			96.01			96.55		
P _{accuracy}	87.77			46.71			46.63			46.77			47.04		

with a spatial resolution of 1.3 m per pixel and a spectral coverage ranging from 0.43 to 0.86 μm with a spectral resolution of 4 nm (12 most noisy channels were removed before experiments). Nine classes of interest plus BKG class, class 0, are considered for this image. The VD estimated for this scene was 14 for UBS to select 14 bands. Since this scene was acquired in a visible range, BREP may not be effective as it worked for the other two image scenes, Purdue Indian Pines

and Salinas. In this case, we used CBEP instead of BREP to generate nonlinear band images. Fig. 12(a)–(c) shows the University of Pavia image, the three-band color composite, and the ground-truth class labels, respectively. The second-order autocorrelated bands: x^2 (14 bands); the third-order autocorrelated bands: x^3 (14 bands), the second cross-correlated bands: xy ($\binom{14}{2} = 91$ bands), and the third-order correlated bands: x^2y ($\binom{14}{2} = 91$ bands), xy^2 ($\binom{14}{2} = 91$ bands)

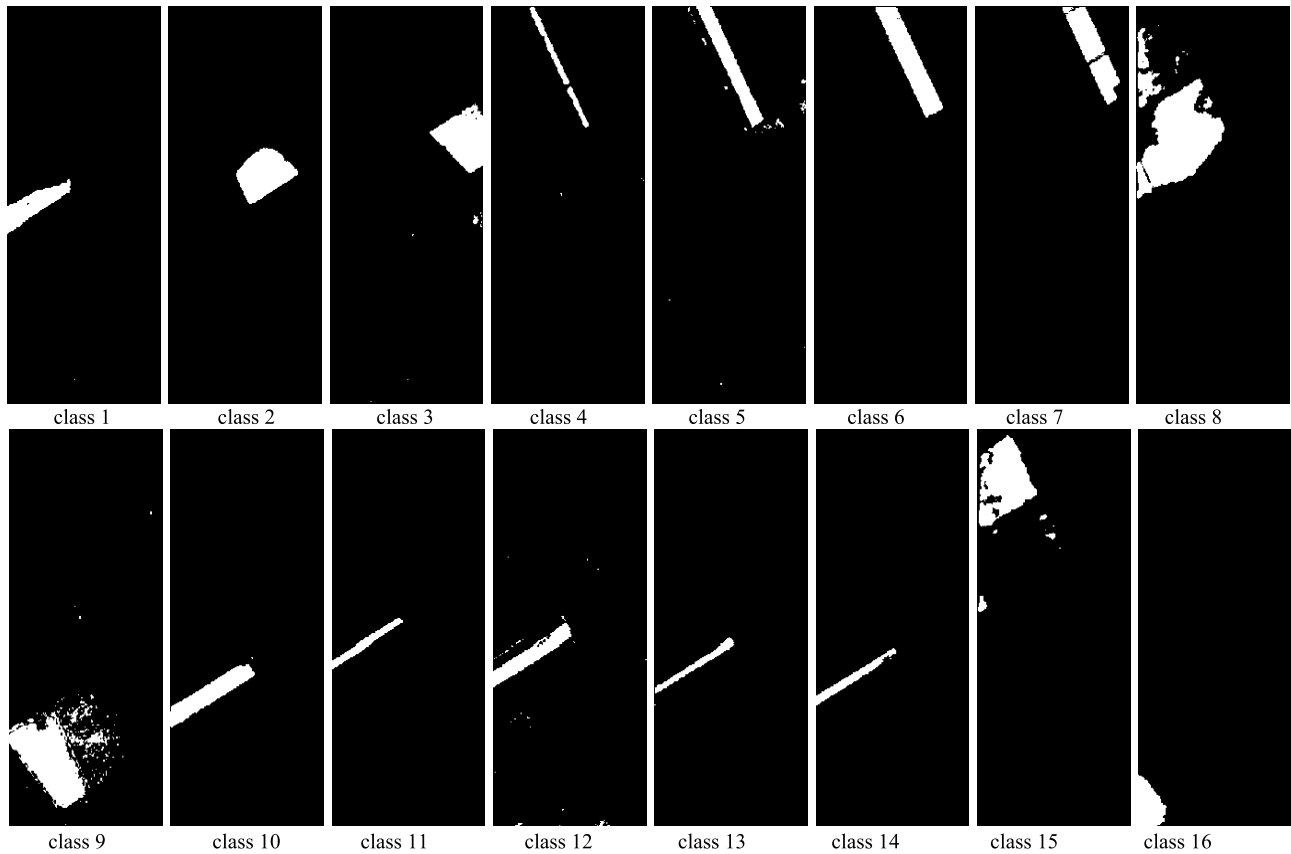


Fig. 10. 16 ICEM-detection abundance fractional class maps in Fig. 9 thresholded by Otsu's method.

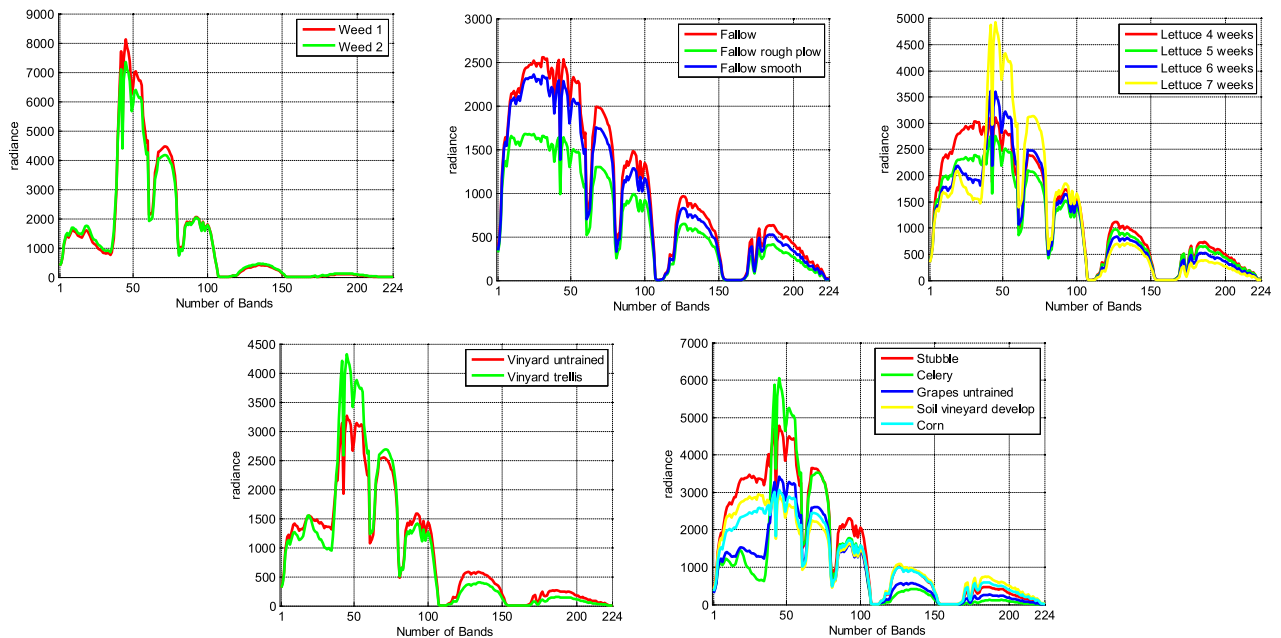


Fig. 11. Spectral profiles of 16 class sample means in the Salinas scene.

bands), and xyz ($\binom{14}{3} = 364$ bands); $\log x$ (14 bands); and \sqrt{x} (14 bands). A total number of nonlinear expanded bands is 693 bands. Table XV tabulates the specifications of parameters and various methods used by BSNE-ICEM. Fig. 13 shows nine ICEM-detection real-valued class maps obtained from using $\Omega^{(0)}$, and Fig. 14 shows their binary maps obtained by applying Otsu's thresholding method to the real-valued class

maps in Fig. 13. Fig. 15 also plots the spectral profiles of the nine classes where spectral signatures are plotted by class means.

Compared with Figs. 7 and 11, which can be separated into four and five different distinct spectral classes, Fig. 15 shows that the spectral profiles of all nine class means in the University of Pavia are very close. So, unlike Tables III and IX,

TABLE XI
PERFORMANCE EVALUATION COMPARISON AMONG BS-SVM-EPF-BASED METHODS FOR THE SALINAS SCENE

Class	BS-SVM-EPF-B-g			BS-SVM-EPF-B-c			BS-SVM-EPF-G-g			BS-SVM-EPF-G-c		
	$P_D\%$	$P_F\%$	$P_{precision}\%$									
1	100.00	0.66	73.64	100.00	0.64	74.27	100.00	0.65	73.83	100.00	0.81	69.49
2	100.00	3.34	50.94	100.00	3.21	51.94	100.00	3.23	51.76	100.00	3.47	49.97
3	100.00	12.61	12.55	100.00	14.40	11.17	100.00	13.41	11.90	100.00	13.94	11.50
4	99.71	5.29	19.33	99.71	4.29	22.82	99.78	3.97	24.19	100.00	3.93	24.44
5	99.40	2.00	55.11	98.99	4.02	37.80	99.10	5.03	32.73	99.29	1.50	62.07
6	100.00	0.93	79.92	100.00	0.85	81.28	100.00	0.86	81.11	100.00	0.93	79.96
7	100.00	0.87	79.34	100.00	0.83	80.12	100.00	0.83	80.00	100.00	0.84	79.82
8	87.61	1.76	84.88	66.44	1.43	84.03	92.23	3.81	73.19	92.20	2.31	81.85
9	100.00	13.42	30.59	99.94	10.69	35.59	100.00	11.85	33.28	100.00	13.44	30.56
10	96.25	1.42	67.34	96.13	1.90	60.54	95.15	1.21	70.49	98.23	2.11	58.61
11	99.63	3.35	22.40	98.78	2.69	26.27	98.78	2.79	25.58	100.00	2.80	25.71
12	100.00	6.12	22.38	100.00	6.64	21.01	100.00	6.04	22.62	100.00	6.52	21.30
13	99.89	0.39	67.83	99.89	0.42	66.26	98.69	0.39	67.61	99.24	0.40	67.48
14	99.72	0.43	69.29	99.44	0.42	69.82	99.25	0.46	67.90	100.00	0.46	67.72
15	89.53	1.71	78.52	88.66	4.22	59.50	63.72	1.20	78.79	84.18	1.03	85.14
16	99.67	0.83	66.56	99.39	0.77	68.21	99.67	0.80	67.30	100.00	0.49	77.16
P_{OA}	95.72			91.13			93.09			96.10		
$P_{accuracy}$	46.64			44.40			45.35			46.82		

TABLE XII
PERFORMANCE EVALUATION COMPARISON AMONG BSNE-SVM-EPF-BASED METHODS FOR THE SALINAS SCENE

Class	BSNE-SVM-EPF-B-g			BSNE-SVM-EPF-B-c			BSNE-SVM-EPF-G-g			BSNE-SVM-EPF-G-c		
	$P_D\%$	$P_F\%$	$P_{precision}\%$									
1	100.00	0.57	76.48	100.00	0.58	75.95	100.00	0.57	76.39	100.00	0.71	72.11
2	99.60	0.56	86.04	99.73	0.63	84.57	99.81	0.64	84.33	100.00	0.78	81.62
3	100.00	12.01	13.10	89.42	12.34	11.60	100.00	11.96	13.15	100.00	11.36	13.75
4	100.00	2.66	32.30	99.71	2.60	32.78	99.86	2.58	32.97	100.00	2.94	30.19
5	98.77	0.81	75.01	99.59	1.42	63.33	99.48	0.89	73.47	99.03	0.72	77.30
6	100.00	0.81	82.05	100.00	0.81	82.05	100.00	0.82	81.80	100.00	0.85	81.23
7	99.27	0.70	82.59	99.47	0.72	82.24	99.53	0.72	82.17	99.69	0.72	82.14
8	91.12	3.96	72.23	89.90	3.17	76.18	86.22	2.27	81.09	86.27	2.15	81.93
9	99.87	14.59	28.82	100.00	15.68	27.38	99.97	14.55	28.89	100.00	15.80	27.23
10	97.59	2.46	54.70	94.14	1.59	64.35	97.25	1.52	66.05	98.20	1.45	67.29
11	100.00	7.00	12.18	99.91	5.53	14.91	100.00	7.15	11.95	100.00	6.06	13.81
12	100.00	0.43	80.26	100.00	1.05	62.65	100.00	0.55	76.23	100.00	0.89	66.56
13	99.67	0.43	65.64	98.58	0.40	67.39	99.89	0.44	65.26	100.00	0.48	63.52
14	99.25	0.46	67.95	99.81	0.52	65.16	99.35	0.45	68.27	99.91	0.41	70.14
15	58.10	0.59	87.40	69.83	1.04	82.45	78.85	1.76	75.79	82.98	1.65	77.88
16	100.00	8.95	15.59	100.00	8.51	16.27	100.00	9.11	15.37	100.00	8.73	15.92
P_{OA}	92.21			92.99			94.03			94.68		
$P_{accuracy}$	44.92			45.31			45.81			46.13		

TABLE XIII
PERFORMANCE EVALUATION COMPARISON AMONG MLC-EPF-BASED METHODS FOR THE SALINAS SCENE

Class	MLC-EPF-B-g			MLC-EPF-B-c			MLC-EPF-G-g			MLC-EPF-G-c		
	$P_D\%$	$P_F\%$	$P_{precision}\%$									
1	100.00	0.15	58.97	93.48	0.14	59.72	97.83	0.13	62.50	100.00	0.12	63.89
2	92.51	4.43	60.35	93.00	4.20	61.74	91.95	4.27	61.07	91.88	4.00	62.63
3	71.81	3.15	48.34	72.53	3.24	47.89	72.53	3.28	47.63	71.69	3.08	48.89
4	100.00	0.96	54.23	100.00	0.91	55.63	100.00	0.95	54.61	99.58	0.90	55.66
5	65.84	2.36	39.60	65.84	2.35	39.70	65.84	2.42	38.97	65.84	2.33	39.90
6	100.00	6.51	35.58	100.00	6.43	35.87	100.00	6.52	35.54	100.00	6.46	35.77
7	100.00	0.17	44.44	100.00	0.14	49.12	100.00	0.13	50.00	100.00	0.09	59.57
8	100.00	1.57	59.75	100.00	1.74	57.25	100.00	1.47	61.20	100.00	1.35	63.23
9	100.00	0.08	54.05	95.00	0.05	65.52	95.00	0.07	57.58	85.00	0.03	73.91
10	98.35	4.94	49.10	98.05	4.89	49.30	98.05	4.89	49.30	97.74	4.91	49.12
11	73.65	5.47	64.02	73.56	5.35	64.52	73.97	5.27	64.97	76.05	5.07	66.46
12	81.79	3.93	37.66	82.46	3.78	38.78	83.47	3.74	39.29	82.29	4.06	37.03
13	100.00	0.63	61.01	100.00	0.62	61.19	99.51	0.61	61.82	99.51	0.60	62.20
14	90.43	14.97	27.88	90.36	15.38	27.32	90.43	15.09	27.73	90.43	15.54	27.14
15	99.48	11.13	14.32	100.00	11.22	14.29	100.00	11.49	14.00	99.22	11.66	13.73
16	98.92	0.29	60.13	98.92	0.27	61.74	98.92	0.34	56.10	92.47	0.35	53.75
P_{OA}	86.33			86.42			86.45			86.66		
$P_{accuracy}$	42.08			42.13			42.14			42.24		

which use the same value for all classes, it is anticipated that the values of parameters would require judicious selection, as shown in Table XV, which must be adapted to various classes.

Table XVI tabulates the results produced by BSNE-ICEM, EPF-B-g, EPF-B-c, EPF-G-g, and EPF-G-c using five performance measures, P_D in (7), P_F in (6), $P_{precision}$ in (9), P_{OA} in (11) and (12), and $P_{accuracy}$ in (15) in terms of percentile (%)

TABLE XIV
PERFORMANCE EVALUATION COMPARISON AMONG BS-MLC-EPF-BASED METHODS FOR THE SALINAS SCENE

Class	BS-MLC-EPF-B-g			BS-MLC-EPF-B-c			BS-MLC-EPF-G-g			BS-MLC-EPF-G-c		
	$P_D\%$	$P_F\%$	$P_{\text{precision}}\%$									
1	97.83	0.14	60.81	93.48	0.13	60.56	97.83	0.12	63.38	100.00	0.11	65.71
2	85.99	4.11	60.37	86.20	4.18	60.02	84.31	4.13	59.81	82.07	4.22	58.63
3	46.39	1.58	54.69	46.99	1.57	55.16	47.35	1.69	53.54	46.14	1.69	52.90
4	97.89	1.22	47.74	100.00	1.21	48.47	91.98	1.15	47.70	87.76	1.20	45.51
5	65.01	2.40	38.96	65.63	2.46	38.52	65.22	2.51	37.95	65.42	2.54	37.75
6	100.00	7.55	32.26	100.00	7.46	32.55	100.00	7.69	31.88	100.00	7.50	32.42
7	100.00	0.24	35.90	100.00	0.24	35.44	100.00	0.22	37.33	100.00	0.20	40.58
8	100.00	1.82	56.10	100.00	1.89	55.13	100.00	1.71	57.66	100.00	1.60	59.23
9	90.00	0.26	24.66	75.00	0.08	46.88	100.00	0.29	24.69	90.00	0.22	27.69
10	82.00	6.14	39.30	78.09	6.15	38.10	77.67	6.25	37.60	75.62	6.34	36.62
11	50.22	2.92	69.46	50.31	2.97	69.11	49.82	2.82	70.05	50.31	3.10	68.19
12	76.39	6.40	25.72	76.22	6.48	25.46	76.22	6.25	26.14	75.72	6.06	26.60
13	100.00	1.26	43.90	100.00	1.20	45.15	100.00	1.28	43.43	100.00	1.17	45.76
14	90.91	14.05	29.28	90.59	14.32	28.83	90.67	14.21	29.01	90.28	14.47	28.54
15	92.75	15.18	10.26	95.85	15.12	10.60	93.52	15.26	10.28	95.60	15.49	10.35
16	97.85	0.55	43.96	98.92	0.46	48.68	98.92	0.64	40.89	96.77	0.64	40.18
P_{OA}	75.57			75.40			74.80			74.19		
P_{accuracy}	36.84			36.76			36.46			36.17		

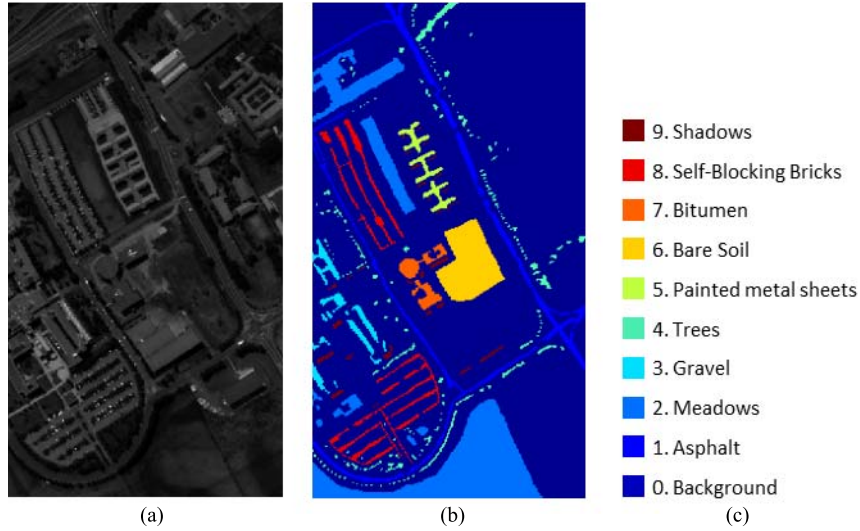


Fig. 12. Ground truth of the University of Pavia scene with nine classes.

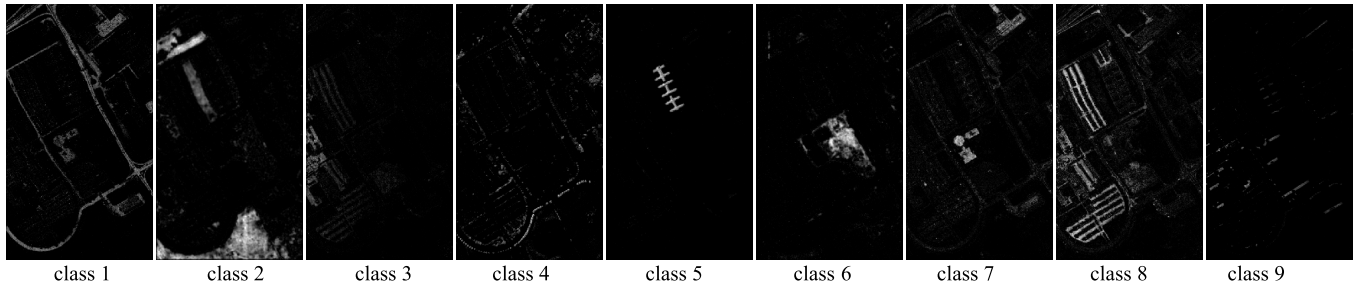


Fig. 13. ICEM nine detection abundance fractional class maps from original bands expanded from uniformly selected 14 bands by band cross-correlation bands (693 bands) for the University of Pavia scene.

where $P_D\%$, $P_F\%$, and $P_{\text{precision}}\%$ are shown in the three columns under each method, and P_{OA} and P_{accuracy} are shown in the last two rows with the bold faced values indicating the best results. If we further plot the spectral profiles of the nine classes by their class means, all spectral signatures are very similar. This fact was evidenced in the last row in Table XVI where P_{accuracy} values produced by four EPF-based methods

were only around 20.40% even though their P_{OA} can be as high as around 99%. This indicates that P_{OA} did not reflect the difficulty of classifying these nine classes. Instead, P_{accuracy} should be the one to be used to measure the class classification difficulty.

Despite the fact that the University of Pavia scene is quite different from the Purdue Indian Pines and Salinas

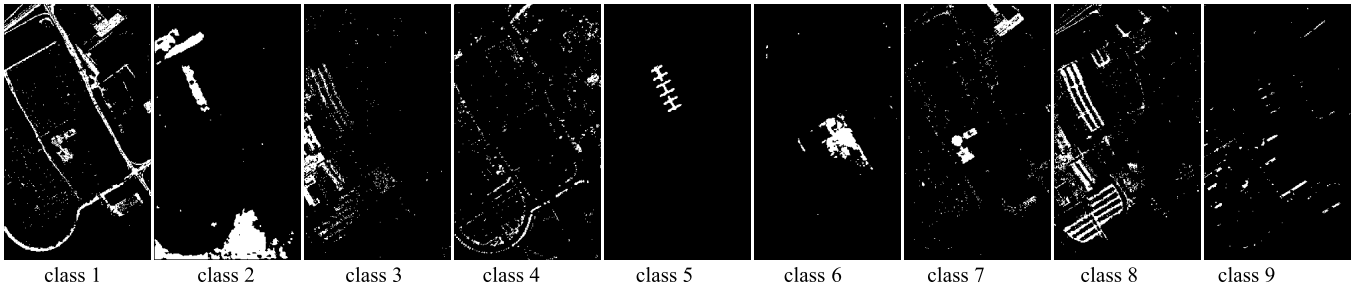


Fig. 14. Nine ICEM-detection abundance fractional class maps in Fig. 13 thresholded by Otsu’s method.

TABLE XV
SPECIFICATIONS OF PARAMETERS USED BY BSNE-ICEM

Band selection method	UBS (14 bands)								
Nonlinear expanded bands	CREP (693 bands)								
d	Class sample mean								
Class #	1	2	3	4	5	6	7	8	9
Iteration #	7	7	2	3	2	12	2	2	3
Gaussian window size	11×11								
σ used in Gaussian filter	0.35	0.60	0.45	0.30	0.45	0.40	0.50	0.50	0.35
Thresholding method	Otsu’s method								
stopping threshold (TI)	0.90	0.90	0.90	0.90	0.90	0.95	0.85	0.72	0.90

TABLE XVI

CLASSIFICATION ACCURACIES FOR ICEM IN COMPARISON WITH EPF-B-c, EPF-B-g, EPF-G-c, and EPF-G-g FOR THE UNIVERSITY OF PAVIA SCENE

Class	BSNE-ICEM			EPF-B-g			EPF-B-c			EPF-G-g			EPF-G-c		
	$P_D\%$	$P_F\%$	$P_{precision}\%$	$P_D\%$	$P_F\%$	$P_{precision}\%$	$P_D\%$	$P_F\%$	$P_{precision}\%$	$P_D\%$	$P_F\%$	$P_{precision}\%$	$P_D\%$	$P_F\%$	$P_{precision}\%$
1	78.21	5.88	32.09	97.07	16.71	18.28	97.10	16.82	18.20	96.53	16.25	18.56	96.95	16.13	18.72
2	78.40	1.06	87.49	98.10	20.22	36.51	98.09	20.26	36.48	98.13	19.63	37.10	98.16	19.32	37.42
3	54.41	2.65	24.63	91.47	1.83	34.19	91.71	1.81	34.55	91.76	1.76	35.11	91.81	1.77	35.02
4	71.02	2.39	30.56	95.04	14.64	10.03	93.99	14.64	9.93	94.35	14.20	10.21	98.14	14.02	10.69
5	94.77	0.15	79.87	100.00	0.88	42.92	100.00	0.82	44.42	100.00	0.92	41.81	100.00	0.82	44.63
6	69.43	0.57	74.60	100.00	30.14	9.69	100.00	29.92	9.74	100.00	29.96	9.73	100.00	30.02	9.72
7	52.98	2.04	23.05	100.00	0.99	39.82	100.00	1.01	39.19	100.00	0.94	40.82	100.00	0.92	41.34
8	72.88	5.90	22.86	99.02	8.15	19.19	98.72	8.10	19.23	98.91	8.09	19.28	99.51	8.13	19.31
9	78.14	0.76	31.52	100.00	4.62	9.41	100.00	4.77	9.15	100.00	6.05	7.44	100.00	6.49	7.00
P_{OA}	73.81			98.97			98.95			98.84			99.17		
$P_{accuracy}$	76.38			20.41			20.41			20.39			20.45		

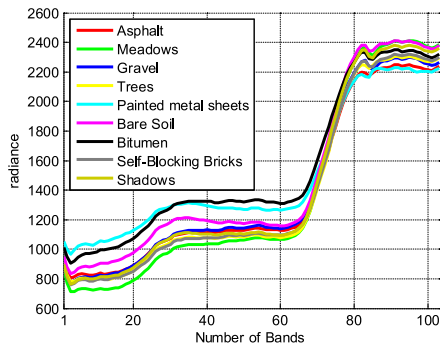


Fig. 15. Spectral profiles of nine class sample means in the University of Pavia scene.

scenes in the sense of spectral range and spectral signature profiles, the results in Table XVI showed similar trends to but were worse than the results in Tables IV and X. According to Table XVI, the best P_{OA} was the one produced by EPF-G-c, while the best $P_{accuracy} = 76.38$ was produced by BSNE-ICEM, which was more than three times better than around 20% produced by four EPF-based methods. As for the other three performance measures, P_D , P_F , and $P_{precision}$, EPF-G-c generally produced the best P_D values for eight out

of nine classes, and BSNE-ICEM produced the best values of P_F and $P_{precision}$ almost across board except two classes, class 3 and class 7 whose best values of P_F and $P_{precision}$ were produced by EPF-G-g and EPF-G-c, respectively. On the other hand, BSNE-ICEM was the best to produce the best values of P_F , $P_{precision}$, and $P_{accuracy}$. The same conclusions drawn from the experiments conducted for the Purdue Indian Pines scene and Salinas scene were also applied to BSNE-ICEM, which is generally the best classification technique to deal with correct and classification and misclassification issues.

Analogous to the Purdue Indian Pines and Salinas scenes, we also implemented four EPF-based methods and MLC for the University of Pavia using the same bands selected by BS and BSNE that were used by BSNE-ICEM. As expected, their respective results tabulated in Tables XVII–XX were also not as good as the results in Table XVI.

D. Parameter Analysis

When ICEM is implemented, three parameters, window size, standard deviation, σ and window size used by a Gaussian filter are specified to capture spatial information and an error threshold ϵ is also used for TI to terminate ICEM.

TABLE XVII
PERFORMANCE EVALUATION COMPARISON AMONG BS-EPF-BASED METHODS FOR THE UNIVERSITY OF PAVIA SCENE

Class	BS-SVM-EPF-B-g			BS-SVM-EPF-B-c			BS-SVM-EPF-G-g			BS-SVM-EPF-G-c		
	$P_D\%$	$P_F\%$	$P_{\text{precision}}\%$									
1	94.51	13.47	18.81	97.03	15.43	17.20	97.84	13.79	18.99	98.72	14.21	18.67
2	96.35	16.28	36.90	96.78	17.23	35.69	95.73	18.48	33.86	98.89	18.50	34.56
3	96.62	3.71	21.03	96.52	1.77	35.76	96.67	3.56	21.75	95.90	3.03	24.44
4	96.48	13.86	9.45	94.88	12.85	9.97	95.27	12.84	10.01	98.69	13.48	9.89
5	100.00	1.20	35.24	100.00	0.86	43.28	100.00	1.14	36.37	99.93	0.76	46.27
6	100.00	21.77	10.25	100.00	22.87	9.80	99.86	21.31	10.43	100.00	18.64	11.76
7	100.00	1.47	30.58	100.00	1.52	29.75	100.00	1.43	31.10	100.00	1.39	31.65
8	97.34	6.91	20.30	98.70	7.36	19.51	97.31	4.82	26.72	98.26	5.95	22.99
9	100.00	4.17	9.91	99.89	2.98	13.34	100.00	5.58	7.59	100.00	6.60	6.50
P_{OA}	96.91			97.48			97.05			98.87		
P_{accuracy}	19.99			20.11			20.02			20.39		

TABLE XVIII
PERFORMANCE EVALUATION COMPARISON AMONG BSNE-EPF-BASED METHODS FOR THE UNIVERSITY OF PAVIA SCENE

Class	BSNE-SVM-EPF-B-g			BSNE-SVM-EPF-B-c			BSNE-SVM-EPF-G-g			BSNE-SVM-EPF-G-c		
	$P_D\%$	$P_F\%$	$P_{\text{precision}}\%$									
1	97.60	16.51	16.33	97.83	14.12	18.62	98.31	14.53	18.26	94.06	14.56	17.58
2	96.96	18.23	34.44	94.71	21.91	29.92	97.13	21.52	30.85	95.92	15.47	37.98
3	97.76	2.66	27.31	95.95	2.45	28.57	95.14	2.72	26.37	95.28	3.62	21.22
4	95.23	14.34	9.06	94.58	12.92	9.89	93.93	13.08	9.72	93.73	12.65	10.00
5	99.93	1.63	28.63	100.00	2.74	19.26	100.00	2.74	19.26	100.00	1.76	27.00
6	99.98	19.00	11.57	99.44	16.39	13.11	99.44	16.71	12.88	100.00	24.06	9.36
7	99.32	0.97	39.80	100.00	1.43	31.03	99.92	1.01	39.07	99.85	1.60	28.69
8	97.39	5.83	23.18	97.58	6.94	20.26	98.37	7.14	19.94	97.72	6.58	21.17
9	99.47	3.70	10.98	99.47	4.40	9.39	99.58	3.63	11.19	97.78	2.63	14.56
P_{OA}	97.59			96.48			97.60			96.37		
P_{accuracy}	20.13			19.90			20.13			19.88		

TABLE XIX
PERFORMANCE EVALUATION COMPARISON AMONG MLC-EPF-BASED METHODS FOR THE UNIVERSITY OF PAVIA SCENE

Class	MLC-EPF-B-g			MLC-EPF-B-c			MLC-EPF-G-g			MLC-EPF-G-c		
	$P_D\%$	$P_F\%$	$P_{\text{precision}}\%$									
1	86.31	13.41	17.53	86.67	13.35	17.66	85.36	13.16	17.64	87.27	13.22	17.91
2	88.02	18.59	31.87	87.85	18.61	31.80	88.11	18.04	32.55	88.20	17.85	32.80
3	69.13	4.18	14.45	70.03	4.22	14.52	69.99	4.06	14.97	67.65	4.03	14.66
4	76.47	7.58	13.14	76.86	7.59	13.18	76.44	7.14	13.82	84.04	7.60	14.22
5	100.00	0.48	57.53	100.00	0.48	57.45	100.00	0.51	56.09	100.00	0.47	57.97
6	93.94	23.52	9.03	93.64	23.39	9.05	93.86	23.15	9.15	95.11	23.17	9.26
7	100.00	2.57	20.09	100.00	2.59	19.94	100.00	2.55	20.23	100.00	2.35	21.55
8	81.53	8.97	14.11	81.80	8.76	14.44	83.00	8.97	14.32	82.13	8.87	14.33
9	100.00	5.75	7.39	100.00	6.04	7.06	100.00	7.40	5.84	100.00	7.23	5.97
P_{OA}	87.15			87.19			87.20			88.04		
P_{accuracy}	17.97			17.98			17.98			18.16		

TABLE XX
PERFORMANCE EVALUATION COMPARISON AMONG BS-MLC-EPF-BASED METHODS FOR THE UNIVERSITY OF PAVIA SCENE

Class	BS-MLC-EPF-B-g			BS-MLC-EPF-B-c			BS-MLC-EPF-G-g			BS-MLC-EPF-G-c		
	$P_D\%$	$P_F\%$	$P_{\text{precision}}\%$									
1	90.21	12.50	19.24	91.00	12.41	19.49	89.64	11.99	19.80	91.00	12.15	19.83
2	85.51	22.21	27.56	85.11	22.24	27.44	85.58	21.57	28.16	86.09	21.40	28.44
3	82.23	5.00	14.38	82.85	4.98	14.53	82.42	4.71	15.18	81.23	4.54	15.46
4	78.17	7.94	12.86	78.13	7.96	12.83	78.88	7.43	13.73	83.68	7.83	13.81
5	99.93	0.49	57.31	99.93	0.49	57.24	99.93	0.53	55.33	100.00	0.47	57.90
6	63.83	18.34	7.96	62.97	18.26	7.89	62.50	17.93	7.97	63.09	17.94	8.04
7	100.00	3.44	15.81	100.00	3.48	15.66	99.77	3.35	16.11	99.92	3.19	16.81
8	91.91	9.59	14.76	92.07	9.41	15.03	92.88	10.13	14.22	94.27	10.13	14.39
9	100.00	6.24	6.85	100.00	6.53	6.56	100.00	8.05	5.39	100.00	7.83	5.53
P_{OA}	84.78			84.67			84.70			85.61		
P_{accuracy}	17.49			17.46			17.47			17.66		

Table XXI tabulates the results of P_{OA} and P_{accuracy} produced by BSNE-ICEM using a Gaussian filter window size from 5×5 to 15×15 . As clearly shown in Table XXI, BSNE-ICEM was very robust to the selected Gaussian filter window size. Furthermore, Fig. 16 also plots the results of P_{OA} and P_{accuracy} produced by BSNE-ICEM using a Gaussian filter with σ

TABLE XXI
ROBUSTNESS OF GAUSSIAN FILTER WINDOW SIZE IN THE PROPOSED METHOD BSNE-ICEM

Window size		5×5	7×7	9×9	11×11	13×13	15×15
Indian Pines	P_{OA}	80.91	80.89	80.89	80.89	80.89	80.89
	$P_{accuracy}$	87.55	87.54	87.54	87.54	87.54	87.54
Salinas	P_{OA}	88.93	88.93	88.93	88.93	88.93	88.93
	$P_{accuracy}$	87.77	87.77	87.77	87.77	87.77	87.77
Univ. of Pavia	P_{OA}	73.81	73.81	73.81	73.81	73.81	73.81
	$P_{accuracy}$	76.38	76.38	76.38	76.38	76.38	76.38

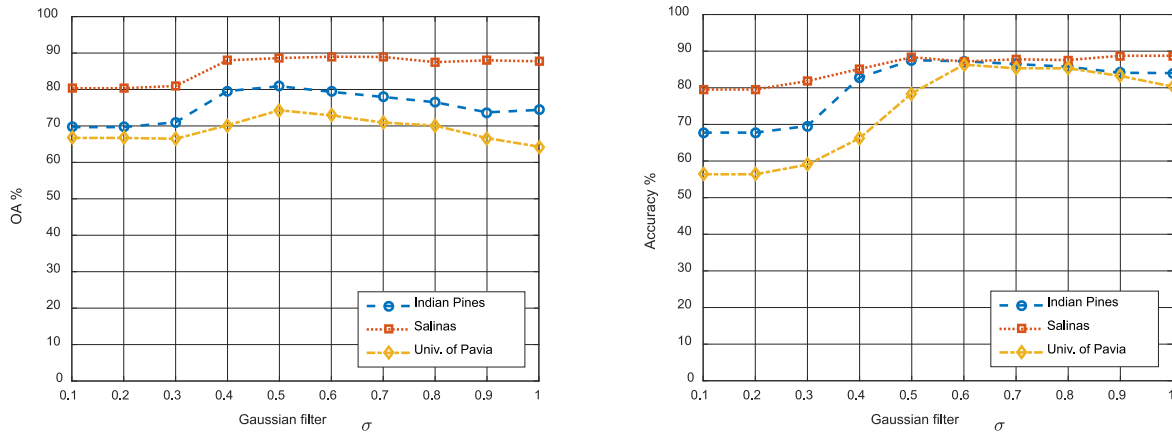


Fig. 16. Performance analysis of P_{OA} and $P_{accuracy}$ using various values of σ .

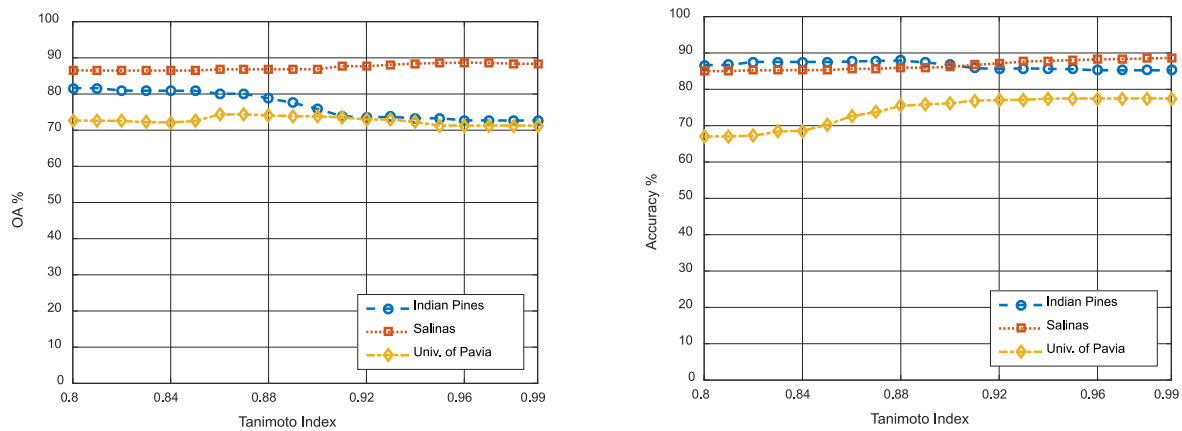


Fig. 17. Various values of error threshold ϵ used by TI as a stopping rule.

varying from 0.1 to 1 where the best performance seemed to be σ in the range from 0.6 to 0.7. Fig. 17 also plots the results of P_{OA} and $P_{accuracy}$ produced by BSNE-ICEM using various values of ϵ for TI as a stopping rule from 0.8 to 0.99. As we can see from Fig. 17, P_{OA} and $P_{accuracy}$ tended to be stable after 0.92.

Despite that the values of TI for different classes for the University of Pavia were selected differently in our experiments, the plots in Fig. 17 were produced by using the same value of TI for all classes to show its robustness to classification once the value of TI goes beyond 0.92. This is because the purpose of Fig. 17 is to illustrate the robustness of TI to classification as the values of TI are increased, and the same value of TI for all classes has sufficiently demonstrated this fact.

E. Discussions

There are four comments, which are noteworthy.

- 1) The Otsu method used in BSNE-ICEM is not necessarily optimal. But it has been shown very effective. However, if there is a better thresholding technique, it can be replaced by this technique.
- 2) The UBS used in BSNE-ICEM is also not necessarily an optimal BS technique, but rather an empirical and simple choice. The performance of BSNE-ICEM can be improved if BS is specifically designed such as band subset selection in [26] and [27].
- 3) The value of the parameter σ used in Gaussian filters is also selected empirically and not optimized. So is the Gaussian window size. Finding optimal values of these

TABLE XXII
COMPUTING TIME IN SECONDS FOR BSNE-ICEM, EPF-BASED METHODS, BS-EPF-BASED METHODS, AND BSNE-EPF-BASED METHODS

Methods	BSNE-ICEM											
Indian Pines	34.30											
Salinas	76.95											
Univ. of Pavia	187.57											
Methods	SVM-EPF											
Input bands	Full bands				Band selection (BS)				Band selection nonlinear extension (BSNE)			
EPF reference	B-g	B-c	G-g	G-c	B-g	B-c	G-g	G-c	B-g	B-c	G-g	G-c
Indian Pines	176.52	178.76	170.61	175.45	25.10	28.56	25.30	29.05	629.03	655.52	618.32	629.94
Salinas	203.91	219.36	208.47	217.34	21.74	36.93	22.16	39.76	421.60	437.80	405.83	425.92
Univ. of Pavia	224.54	263.06	251.21	246.72	54.60	68.32	55.61	73.40	1662.17	1901.18	1848.32	1925.45
Methods	MLC-EPF											
Input bands	Full bands				Band selection (BS)				Band selection nonlinear extension (BSNE)			
EPF reference	B-g	B-c	G-g	G-c	B-g	B-c	G-g	G-c	B-g	B-c	G-g	G-c
Indian Pines	4.58	7.37	4.46	7.69	1.11	4.08	1.07	4.36	-	-	-	-
Salinas	26.04	44.22	29.09	48.94	5.76	21.35	5.51	24.13	-	-	-	-
Univ. of Pavia	14.11	30.06	16.24	35.83	6.11	22.68	6.01	26.74	-	-	-	-

two parameters is challenging, since they are determined by the data to be used for processing. Nevertheless, Table XXI and Fig. 16 show that the empirical selections of parameters, σ , and window size are rather robust.

- 4) The Gaussian filters used in BSNE-ICEM can be replaced with other types of spatial filters if there is one that can do better than Gaussian filters.

F. Contributions

The experiments conducted in Section VII-C have several contributions. First of all, experiments are comprehensive where four EPF-based methods using BS and BSNE and MLC with/without BS are included for comparison. We believe that these results are not available or reported in the literature. Another contribution is new performance measures introduced for performance evaluation. In particular, false-classification rate, P_F , precision rate, $P_{\text{precision}}$, and accuracy rate, P_{accuracy} , are not included as measures in [1]–[13] to evaluate the misclassification rate plus BKG classification. A third contribution is to provide evidence that the detection rate P_D is not equivalent to classification rate. As a result, P_{OA} is not equivalent to P_{accuracy} or $P_{\text{precision}}$. Specifically, detection rate and accuracy rate are not directly correlated. According to (7), detection rate is calculated based on individual classes in which case the BKG class is not counted. By contrast, the precision rate in (9) and accuracy rate in (10) are calculated by all classes including the BKG class. In general, the BKG class always produces worst classification. That is the reason the EPF-based methods which do not account for the BKG class produced very poor precision and accuracy rates.

VIII. COMPUTATIONAL COMPLEXITY ANALYSIS

In order to evaluate the efficiency of BSNE-ICEM compared with four EPF-based methods and MLC, Table XXII tabulates their respective computing times in seconds where a computer environment was specified by an Intel i7-6500U 2.5-GHz base frequency CPU and 12-GB 2133-MHz memory. All experiments were implemented using MATLAB and the SVM available in LIBSVM [28]. In particular, the Gaussian kernel parameter σ and slack variables used by SVM were selected by fivefold cross validation. It should be noted

that ICEM and MLC did not need training sample vectors. To the contrary, the computing timing required by the SVM-EPF methods did include the computing times of training, prediction, principal components analysis (PCA), and EPF. Moreover, the computing time of all the experiments did not include the times of generating inputs, such as desired target generated for ICEM and MLC, generating training sample vectors for SVM, and processing BS and nonlinear extension. As we can see from Table XXII, MLC required the least computing time while EPF-based methods required the most computing time.

IX. CONCLUSION

This paper develops an approach to hyperspectral image classification, which is based on a hyperspectral sub-pixel target detector, CEM, coupled with BS-then-nonlinear expansion (BSNE). It is quite different from the conventional SVM-based spectral-spatial approaches reported in the literature. It reinvents a wheel by replacing SVM with CEM and kernelization used by SVM with BSNE. In order to capture spatial information, Gaussian-filtered CEM-detected abundance fractional maps are fed back iteratively to BSNE band-expanded images to form a new set of hyperspectral cubes, which will be reprocessed by CEM so as to improve classification performance. Such an ICEM can be considered as a spectral-spatial filter, that is, the more the iterations carried out by ICEM, the more the spatial information captured. As a result of BSNE-ICEM, there are many unique features that can be derived as follows.

- 1) CEM operating as a subpixel detector can be used to replace the commonly used SVM as the pure-pixel classification technique.
- 2) CEM-detection abundance fractional maps can be thresholded, such as Otsu's method, to produce binary maps to perform classification.
- 3) Using a one-against-rest strategy for a binary hypothesis testing problem converts a multiclassification confusion matrix to a binary confusion matrix. As a result, three new performance measures, such as detection rate, false classification rate, and precision rate, are introduced in addition to the commonly used OA and accuracy.
- 4) The idea of taking advantage of iterative feedbacks from Gaussian filtered CEM detection abundance fractional

maps captures spatial information that can also be applied to many other pixel-based spectral filters.

- 5) Opens up a new direction for hyperspectral image classification. Several investigations along this line are currently undertaken.

ACKNOWLEDGMENT

The authors would like to thank Dr. X. Kang for sharing his codes available at Web site <http://xudongkang.weebly.com>.

REFERENCES

- [1] F. Melgani and L. Bruzzone, "Classification of hyperspectral remote sensing images with support vector machines," *IEEE Trans. Geosci. Remote Sens.*, vol. 42, no. 8, pp. 1778–1790, Aug. 2004.
- [2] J. A. Benediktsson, J. A. Palmason, and J. R. Sveinsson, "Classification of hyperspectral data from urban areas based on extended morphological profiles," *IEEE Trans. Geosci. Remote Sens.*, vol. 43, no. 3, pp. 480–491, Mar. 2005.
- [3] G. Camps-Valls and L. Bruzzone, "Kernel-based methods for hyperspectral image classification," *IEEE Trans. Geosci. Remote Sens.*, vol. 43, no. 6, pp. 1351–1362, Jun. 2005.
- [4] Y. Tarabalka, J. A. Benediktsson, and J. Chanussot, "Spectral–spatial classification of hyperspectral imagery based on partitional clustering techniques," *IEEE Trans. Geosci. Remote Sens.*, vol. 47, no. 8, pp. 2973–2987, Aug. 2009.
- [5] Y. Tarabalka, M. Fauvel, J. Chanussot, and J. A. Benediktsson, "SVM- and MRF-based method for accurate classification of hyperspectral images," *IEEE Geosci. Remote Sens. Lett.*, vol. 9, no. 4, pp. 736–740, Oct. 2010.
- [6] J. Li, J. M. Bioucas-Dias, and A. Plaza, "Semisupervised hyperspectral image segmentation using multinomial logistic regression with active learning," *IEEE Trans. Geosci. Remote Sens.*, vol. 48, no. 11, pp. 4085–4098, Nov. 2010.
- [7] B. Zhang, S. Li, X. Jia, L. Gao, and M. Peng, "Adaptive Markov random field approach for classification of hyperspectral imagery," *IEEE Geosci. Remote Sens. Lett.*, vol. 8, no. 11, pp. 4085–4098, Nov. 2011.
- [8] J. Li, J. M. Bioucas-Dias, and A. Plaza, "Hyperspectral image segmentation using a new Bayesian approach with active learning," *IEEE Trans. Geosci. Remote Sens.*, vol. 49, no. 10, pp. 3947–3960, Oct. 2011.
- [9] Y. Chen, N. Nasrabadi, and T. D. Tran, "Hyperspectral image classification using dictionary-based sparse representation," *IEEE Trans. Geosci. Remote Sens.*, vol. 49, no. 10, pp. 3973–3985, Oct. 2011.
- [10] Y. Tarabalka, M. Fauvel, J. Chanussot, and J. A. Benediktsson, "Segmentation and classification of hyperspectral images using minimum spanning forest grown from automatically selected markers," *IEEE Trans. Syst., Man, Cybern. B*, vol. 40, no. 5, pp. 1267–1279, Oct. 2011.
- [11] M. Fauvel, Y. Tarabalka, J. A. Benediktsson, J. Chanussot, and J. C. Tilton, "Advances in spectral-spatial classification of hyperspectral images," *Proc. IEEE*, vol. 101, no. 3, pp. 652–675, Mar. 2013.
- [12] X. Kang, S. Li, and J. A. Benediktsson, "Spectral–spatial hyperspectral image classification with edge-preserving filtering," *IEEE Trans. Geosci. Remote Sens.*, vol. 52, no. 5, pp. 2666–2677, May 2014.
- [13] X. Guo, X. Huang, L. Zhang, L. Zhang, A. Plaza, and J. A. Benediktsson, "Support tensor machines for classification of hyperspectral remote sensing imagery," *IEEE Trans. Geosci. Remote Sens.*, vol. 54, no. 6, pp. 3248–3264, Jun. 2016.
- [14] C.-I. Chang, *Hyperspectral Data Processing: Algorithm Design and Analysis*. Hoboken, NJ, USA: Wiley, 2013.
- [15] J. C. Harsanyi, "Detection and classification of subpixel spectral signatures in hyperspectral image sequences," Ph.D. dissertation, Dept. Elect. Eng., Univ. Maryland, Baltimore County, MD, USA, Aug. 1993.
- [16] W. Farrand and J. C. Harsanyi, "Mapping the distribution of mine tailings in the Coeur d'Alene River Valley, Idaho, through the use of a constrained energy minimization technique," *Remote Sens. Environ.*, vol. 59, no. 1, pp. 64–76, 1997.
- [17] C.-I. Chang, "Target signature-constrained mixed pixel classification for hyperspectral imagery," *IEEE Trans. Geosci. Remote Sens.*, vol. 40, no. 5, pp. 1065–1081, May 2002.
- [18] C.-I. Chang, *Hyperspectral Imaging: Techniques for Spectral Detection and Classification*. Norwell, MA, USA: Kluwer, 2003.
- [19] H. Ren and C.-I. Chang, "A generalized orthogonal subspace projection approach to unsupervised multispectral image classification," *IEEE Trans. Geosci. Remote Sens.*, vol. 38, no. 6, pp. 2515–2528, Nov. 2000.
- [20] N. Otsu, "A threshold selection method from gray-level histogram," *IEEE Trans. Syst., Man, Cybern.*, vol. SMC-9, no. 1, pp. 62–66, Jan. 1979.
- [21] J. R. Jensen, *Introductory Digital Image Processing: A Remote Sensing Perspective*, 2nd ed. Upper Saddle River, NJ, USA: Prentice-Hall, 1996.
- [22] H. Ren and C.-I. Chang, "A computer-aided detection and classification method for concealed targets in hyperspectral imagery," in *Proc. IEEE Int. Geosci. Remote Sens. Symp.*, Seattle, WA, USA, Jul. 1998, pp. 1016–1018.
- [23] S. Theodoridis and K. Koutroumbas, *Pattern Recognition*. Orlando, FL, USA: Academic, 1999, p. 366.
- [24] D. A. Langrebe, *Signal Theory Methods in Multispectral Remote Sensing*. Hoboken, NJ, USA: Wiley, 2003.
- [25] C.-I. Chang and Q. Du, "Estimation of number of spectrally distinct signal sources in hyperspectral imagery," *IEEE Trans. Geosci. Remote Sens.*, vol. 42, no. 3, pp. 608–619, Mar. 2004.
- [26] H. C. Li, C.-I. Chang, Y. Li, and L. Wang, "Constrained multiple band selection for hyperspectral imagery," in *Proc. IEEE Geosci. Remote Sens. Symp.*, Beijing, China, Jul. 2016, pp. 6149–6152.
- [27] L. Wang and C.-I. Chang, "Multiple band selection for anomaly detection in hyperspectral imagery," in *Proc. IEEE Geosci. Remote Sens. Symp.*, Beijing, China, Jul. 2016, pp. 7022–7025.
- [28] C. C. Chang and C. J. Lin, "LIBSVM: A library for support vector machines," *ACM Trans. Intell. Syst. Technol.*, vol. 2, no. 3, pp. 27:1–27:27, Apr. 2011. [Online]. Available: <http://www.csie.ntu.edu.tw/~cjlin/libsvm>



Bai Xue (S'15) received the B.E. degree in automation from the Huazhong University of Science and Technology, Wuhan, China, in 2015. He is currently pursuing the Ph.D. degree in electrical engineering with the University of Maryland, Baltimore County, Baltimore, MD, USA.



From 2014 to 2015, he was a Program Exchange Undergraduate Student with the Department of Electrical and Computer Engineering, University of Detroit Mercy, Detroit, MI, USA. He is also a Visiting Research Assistant with the Center for Hyperspectral Imaging in Remote Sensing, Dalian Maritime University, Dalian, China. His research interests include multispectral/hyperspectral imaging, pattern recognition, medical imaging, and medical data analysis.

Chunyan Yu (M'17) received the B.Sc. and Ph.D. degrees in environment engineering from Dalian Maritime University, Dalian, China, in 2004 and 2012, respectively.

In 2004, she joined the College of Computer Science and Technology, Dalian Maritime University. From 2013 to 2016, she was a Post-Doctoral Fellow with the Information Science and Technology College, Dalian Maritime University. From 2014 to 2015, she was a Visiting Scholar with the College of Physicians and Surgeons, Columbia University, New York City, NY, USA. She is currently a Lecturer with the Information Science and Technology College, Dalian Maritime University. Her research interests include image segmentation, hyperspectral image classification, and pattern recognition.



Yulei Wang received the B.S. degree in signal and information processing from Harbin Engineering University, Harbin, China, in 2009, and the joint Ph.D. degree in signal and information processing from Harbin Engineering University and the Remote Sensing Signal and Image Processing Laboratory, University of Maryland, Baltimore County, Baltimore, MD, USA, in 2015.

She is currently a Lecturer with the College of Information Science and Technology, Dalian Maritime University, Dalian, China. Her research interests include hyperspectral image processing and vital signs signal processing. Dr. Wang was a recipient of the China Scholarship Council in 2011 for her joint Ph.D. degree.



Meiping Song received the Ph.D. degree from the College of Computer Science and Technology, Harbin Engineering University, Harbin, China, in 2006.

From 2013 to 2014, she was a Visiting Associate Research Scholar with the University of Maryland, Baltimore County, Baltimore, MD, USA. She is currently an Associate Professor with the College of Information Science and Technology, Dalian Maritime University, Dalian, China. Her research interests include remote sensing and hyperspectral image processing.



Sen Li received the B.S. degree in microelectronics from Liaoning University, Shenyang, China, in 1996, the M.S. degree in information and communication engineering from Dalian Maritime University, Dalian, China, in 1999, and the Ph.D. degree in information and signal processing from the Dalian University of Technology, Dalian, in 2011.

In 2013, she held a postdoctoral position with the Department of Electrical and Computer Engineering, Concordia University, Montreal, QC, Canada. She is currently an Associate Professor with the

Department of Information Science and Technology, Dalian Maritime University. Her research interests include array signal processing, communication signal processing, non-Gaussian signal processing, and hyperspectral image processing.



Lin Wang received the B.S. degree in optoelectronic technology and the M.S. degree in physical electronics from Xidian University, Xi'an, China, in 2000 and 2013, respectively.

From 2015 to 2016, she was a Visiting Research Associate Scholar with the Remote Sensing Signal and Image Processing Laboratory, University of Maryland, Baltimore County, Baltimore, MD, USA. She is currently an Associate Professor with the School of Physics and Optoelectronic Engineering, Xidian University. Her research interests include

hyperspectral image processing, automatic target recognition, and real-time image processing.



Hsian-Min Chen received the Ph.D. degree in electrical engineering from National Chung Hsing University, Taichung, Taiwan, in 2008.

He was a Post-Doctoral Fellow with the Department of Medical Research, China Medical University Hospital, Taichung, from 2008 to 2010. He was the Chairman and an Associate Professor with the Department of Biomedical Engineering, Hungkuang University, Taichung, from 2011 to 2014. He is currently an Associate Research Scientist with the Center for Quantitative Imaging in Medicine,

Department of Medical Research, Taichung Veterans General Hospital, Taichung. His research interests include hyperspectral image processing, hyperspectral medical image processing, and biosignal processing.



Chein-I Chang (S'81–M'87–SM'92–F'10–LF'17) received the B.S. degree in mathematics from Soochow University, Taipei, Taiwan, in 1973, the M.S. degree in mathematics from the Institute of Mathematics, National Tsing Hua University, Hsinchu, Taiwan, in 1975, the M.A. degree in mathematics from Stony Brook University, Stony Brook, NY, USA, in 1977, the M.S. and M.S.E.E. degrees from the University of Illinois at Urbana–Champaign, Urbana, IL, USA, in 1980 and 1982, respectively, and the Ph.D. degree in electrical engineering from

the University of Maryland at College Park, College Park, MD, USA, in 1987.

He was a Visiting Research Specialist with the Institute of Information Engineering, National Cheng Kung University, Tainan, Taiwan, from 1994 to 1995, and a Distinguished Visiting Fellow/Fellow Professor, from 2009 to 2010, both of which were sponsored by the National Science Council, Taiwan. He was the Distinguished Lecturer Chair with National Chung Hsing University from 2005 to 2006, sponsored by the Ministry of Education, Taiwan. He has been a Distinguished Chair Professor with National Chung Hsing University, Taichung, Taiwan, since 2014, and a Chair Professor with Providence University, Taichung, since 2012. He has been with the University of Maryland, Baltimore County, Baltimore, MD, USA, since 1987, where he is currently a Professor with the Department of Computer Science and Electrical Engineering. He is holding the Chang Jiang Scholar Chair Professorship and the Director of the Center for Hyperspectral Imaging in Remote Sensing, Dalian Maritime University, Dalian, China. He is also holding the Hua Shan Scholar Chair Professorship with Xidian University, Xi'an, China. He has seven patents on hyperspectral image processing. He authored four books, such as *Hyperspectral Imaging: Techniques for Spectral Detection and Classification* (Kluwer Academic, 2003), *Hyperspectral Data Processing: Algorithm Design and Analysis* (Wiley, 2013), *Real Time Progressive Hyperspectral Image Processing: Endmember Finding and Anomaly Detection* (Springer, 2016), and *Recursive Hyperspectral Sample and Band Processing: Algorithm Architecture and Implementation* (Springer, 2017). He edited two books, such as *Recent Advances in Hyperspectral Signal and Image Processing* in 2006 and *Hyperspectral Data Exploitation: Theory and Applications* (Wiley, 2007), and co-edited with A. Plaza a book *High Performance Computing in Remote Sensing* (CRC, 2007). His research interests include multispectral/hyperspectral image processing, automatic target recognition, and medical imaging.

Dr. Chang is a Fellow of SPIE. He received the National Research Council Senior Research Associateship Award from 2002 to 2003 sponsored by the U.S. Army Soldier and Biological Chemical Command, Edgewood Chemical and Biological Center, Aberdeen Proving Ground, Maryland. He was a Plenary Speaker for the Society for Photo-Optical Instrumentation Engineers (SPIE) Optics + Applications, Remote Sensing Symposium, in 2009. He was a Keynote Speaker with the User Conference of Hyperspectral Imaging 2010, Industrial Technology Research Institute, Hsinchu; the 2009 Annual Meeting of the Radiological Society of the Republic of China, 2009, Taichung; the 2008 International Symposium on Spectral Sensing Research in 2008; and the Conference on Computer Vision, Graphics, and Image Processing 2003, Kimen and 2013, Nantou, Taiwan. He was an Associate Editor in the area of hyperspectral signal processing of the IEEE TRANSACTIONS ON GEOSCIENCE AND REMOTE SENSING from 2001 to 2007. He was a Guest Editor of a special issue of the *Journal of High Speed Networks on Telemedicine and Applications* in 2000 and a Co-Guest Editor of another special issue of the *Journal of High Speed Networks on Telemedicine and Applications on Broadband Multimedia Sensor Networks in Healthcare Applications* in 2007. He is a Co-Guest Editor of special issues on High Performance Computing of Hyperspectral Imaging for the *International Journal of High Performance Computing Applications* in 2007, Signal Processing and System Design in Health Care Applications of the *EURASIP Journal on Advances in Signal Processing* in 2009, and Multispectral, Hyperspectral, and Polarimetric Imaging Technology of the *Journal of Sensors*. He is currently an Associate Editor of *Artificial Intelligence Research* and also on the editorial boards of the *Journal of High Speed Networks*, *Recent Patents on Mechanical Engineering*, the *International Journal of Computational Sciences and Engineering*, the *Journal of Robotics and Artificial Intelligence*, and the *Open Remote Sensing Journal*.